

Article

LWIR Lateral Effect Position Sensitive HgCdTe Photodetector at 205 K

Jarosław Pawluczyk ^{1,2,*} , Mateusz Żbik ^{2,3} and Józef Piotrowski ²¹ Institute of Applied Physics, Military University of Technology, 00-908 Warsaw, Poland² VIGO Photonics S.A., 05-850 Ozarów Mazowiecki, Poland; mateusz.zbik.dokt@pw.edu.pl (M.Ż.); jpiotr@vigophotonics.com (J.P.)³ Institute of Electronic Systems, Warsaw University of Technology, 00-665 Warsaw, Poland

* Correspondence: jaroslaw.pawluczyk@wat.edu.pl

Abstract: We describe in detail the construction and characterization of a Peltier-cooled long-wavelength infrared (LWIR) position-sensitive detector (PSD) based on the lateral effect. The device was recently reported for the first time to the authors' knowledge. It is a modified PIN HgCdTe photodiode, forming the tetra-lateral PSD, with a photosensitive area of $1 \times 1 \text{ mm}^2$, operating at 205 K in the 3–11 μm spectral range, capable of achieving a position resolution of 0.3–0.6 μm using 10.5 μm 2.6 mW radiation focused on a spot of the $1/e^2$ diameter 240 μm , with a box-car integration time of 1 μs and correlated double sampling.

Keywords: LWIR; HgCdTe; PSD; position-sensing detector; photodetector; lateral effect; tetra-lateral; PIN photodiode; Peltier-cooled

1. Introduction

A position-sensing detector (PSD) is a photosensor that detects the position of a light spot on its surface. A PSD enables precise and fast beam alignment and tracking in a variety of applications [1], such as active beam stabilization, optical remote-control devices, infrared (IR) range finders, target detection and tracking, missile interception, IR countermeasures, optical switches, and measurements of vibrations, distortions, and lens refraction/reflection.

The motivation for the responsivity spectral range of up to 10–11 μm , embracing a significant portion of the LWIR band (wavelength $\lambda = 8\text{--}14 \mu\text{m}$), includes detection and tracking of distant objects, where the LWIR may be preferred to the MWIR ($\lambda = 3\text{--}5 \mu\text{m}$) and a shorter wavelength due to less aerosol scattering and better performance in environments with dust, fog, or winter haze; higher immunity to atmospheric turbulence; and reduced sensitivity to solar glints and fire flares [2] (p. 5).

LWIR PSDs can also be applied in positioning systems with detection in the LWIR band, especially when LWIR laser beams are used, e.g., in optical communication in free space, in industry using high-power CO₂ lasers for hard-material treatment, or in nondestructive inspection and metrology tools. There are numerous medical, industrial, and military applications in the LWIR range [3].

Owing to the frequent requirement for fast and accurate position detection and tracking, PSDs based on fast photon detectors, such as photodiodes, are often preferred to thermal PSDs—quadrant detectors or dense arrays, the acceptable sensitivity of which is achieved at the expense of their slow response times of the order of milliseconds and more [4] (p. 57) [5].

PSDs with the best parameters in terms of position sensitivity and linearity use the lateral photoelectric effect (L-PSD devices) [1,6–8]. L-PSDs are single-element detectors of various types and materials, p-n photodiodes or heterostructures, also field-effect phototransistors, where the built-in or externally supplied electric field, perpendicular to the



Citation: Pawluczyk, J.; Żbik, M.; Piotrowski, J. LWIR Lateral Effect Position Sensitive HgCdTe Photodetector at 205 K. *Sensors* **2023**, *23*, 4915. <https://doi.org/10.3390/s23104915>

Academic Editors: Jun Huang, Fan Fan and Hao Li

Received: 7 February 2023

Revised: 12 April 2023

Accepted: 24 April 2023

Published: 19 May 2023



Copyright: © 2023 by the authors. Licensee MDPI, Basel, Switzerland. This article is an open access article distributed under the terms and conditions of the Creative Commons Attribution (CC BY) license (<https://creativecommons.org/licenses/by/4.0/>).

substrate, enables the separation of photogenerated electrons and holes, which next spread laterally in a resistive layer, which will be described later on [7–9].

The lateral photoelectric effect was originally described by Schottky in 1930 [10], rediscovered and further elaborated by Wallmark in 1957 [11], and described by Lucovsky in 1960 with analytical equations [12], which help interpret the photoelectric effects observed in nonuniformly irradiated p-n junctions. Developments in the field have since been achieved by many researchers, including the optimization of a PSD construction [13,14] and the shape of electrodes in particular [15].

The main advantage of the L-PSD over photon quadrant detectors (QDs) [16,17], which have been used so far as fast Peltier-cooled PSDs for the LWIR band, is that L-PSD performance is much less dependent on the light-spot intensity distribution. In the case of the L-PSD, the lateral extent of the position measurement span corresponds to the side length of the photosensitive area, while in the case of the QD it corresponds to the diameter of the light spot. Hence, the position linearity is much greater for the L-PSD than for the QD for a given photosensitive area. The L-PSD may also replace a linear array detector, e.g., in compact spectrometers [7].

Previous LWIR L-PSD designs have used cryogenic cooling [6], which is common for LWIR detectors, as it reduces their electric charge thermal generation-recombination (G-R) noise below the level determined by the 300 K thermal background, allowing background-limited performance (BLIP). A cryo-cooler, though, makes the detector assembly bulky, expensive, and often less convenient to operate. Therefore, we decided to explore the possibility of position detection of 10–11 μm radiation at a higher operating temperature, ca. 200 K, achievable by Peltier mini-coolers—small, rugged devices with an operating life of about 20 years and a supply power below 2 W. This is perhaps the first demonstration of such an operation, carried out here on a HgCdTe photodiode with a photosensitive area of $1 \times 1 \text{ mm}^2$, large for this spectral range and operating temperature, at reverse bias 0.16 V/50 mA. However, power-consuming cooling and bias are also not desirable for portable and integrated devices.

The current L-PSD performance for the IR range of $\lambda < 2 \mu\text{m}$ (SWIR) may be used as a first benchmark for LWIR PSD development. This includes position resolution of about 0.1 μm normalized to a photosensitive area 1 mm in size, with response times on the order of one to several tens of microseconds and excellent position linearity, with nonlinearity $< 2\%$, obtained without cooling at 0 V bias [1,8,18,19].

SWIR detectors, including L-PSDs, benefit from wide-bandgap semiconductors, used as radiation absorbers. They require neither cooling nor bias to achieve BLIP. SWIR L-PSDs have been commercially available for several decades at a moderate price [9,19]. On the other hand, uncooled or Peltier-cooled LWIR photon detectors suffer from huge thermal generation noise. Their sensitivity is several orders of magnitude lower than that of the wide-gap devices. This is true even for BLIP LWIR detectors, because of the low energy of LWIR photons, about 0.1 eV, comparable to the constant $kT = 0.026 \text{ eV}$ of the Boltzmann distribution at $T = 300 \text{ K}$, resulting in high (300 K) thermal background flux and noise in this spectral range. This is exacerbated by the contribution of nonradiative thermal G-R mechanisms, still playing a role in many LWIR uncooled or Peltier-cooled detectors. The nonradiative high thermal G-R rate in LWIR absorbers results from the low energy of transition of electrons between energy levels, corresponding to the low energy of the absorbed LWIR photons. The thermally generated dark currents of uncooled or Peltier-cooled LWIR photon detectors can be very high if they are not blocked by special barriers in bandgap-engineered structures.

Figure 1 schematically illustrates the principle of operation of the lateral effect photodiode used here. It is a modified PIN photodiode made of LWIR HgCdTe. The inter-band absorption of IR in the absorber layer generates electron–hole pairs, collected as a photocurrent. The device is shaped as a mesa structure, where the lower cathode layer forms the resistive layer acting as the current divider, while the upper anode layer is a common contact. The photocurrent is divided between four cathode metal electrodes in proportion to

the resistances of the photocurrent paths between the illuminated region and the electrodes in one resistive layer. Thus, this is the tetra-lateral type (TL-PSD) of L-PSD [13]. In the applied configuration, a pair of cathode electrodes is extended along the opposite edges of the mesa structure, parallel to each other and perpendicular to the same electrodes of the second pair.

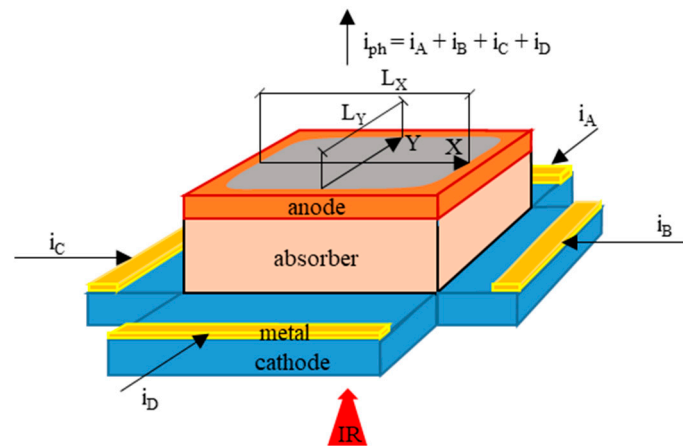


Figure 1. Principle of operation of the PSD tetra-lateral photodiode (adapted with permission from Ref. [20]; copyright: 2022, SPIE). The photosensitive area is in grey. i_A , i_B , i_C , and i_D are the photocurrents flowing to the respective preamplifiers of channels A, B, C, and D.

With Peltier modest cooling to 205 K, the photodiode resistance at 0 V bias is low ($<1 \Omega$) and dominated by the parasitic series resistance, due to the high thermal G-R. The device must be reverse biased to maximize the differential impedance of the photodiode, which is critical to the performance–sensitivity and linearity–of the LWIR L-PSD.

Assuming perfect position linearity, the transverse position (X , Y) of the light spot gravity center is determined by subtracting the signals from the opposite cathode electrodes (channels) and dividing this difference by the sum of these signals (adapted with permission from Ref. [20]; copyright: 2022, SPIE):

$$X_{\text{PSD}} = \frac{i_B - i_C}{i_B + i_C} \times k_X = \frac{U_B - U_C}{U_B + U_C} \times k_X \quad (1)$$

$$Y_{\text{PSD}} = \frac{i_A - i_D}{i_A + i_D} \times k_Y = \frac{U_A - U_D}{U_A + U_D} \times k_Y \quad (2)$$

where X_{PSD} and Y_{PSD} are the Cartesian coordinates of the radiation beam spot position determined from the TL-PSD signals, i.e., the U_A , U_B , U_C , and U_D voltages at respective channel preamplifier outputs. The preamplifiers integrate the photocurrent, giving the output voltage proportional to the input radiation pulse energy. The scale factors k_X and k_Y are proportional to the resistance length $L \approx L_X \approx L_Y \approx 1 \text{ mm}$ (Figure 1). If the dark current of the photodiode is significant, k_X and k_Y are also affected by the dark current and energy of the radiation pulses. In this case, for k_X and k_Y to be constant, the radiation pulse energy should be constant too [7]. The resistance lengths L_X and L_Y represent the linear size of the detector photosensitive area in the X and Y directions, respectively, where the TL-PSD signals change with the respective X and Y position shifts, preferably in linear proportion.

The nonuniformities in the photodiode material layers influence the distribution of the photocurrent between the cathode electrodes and thus cause an error in the light spot position measurement. The position signal error can be corrected using calibration and postprocessing, providing the position measurement noise is low enough. However, time-consuming corrections are not desired in view of the required fast position signal response.

Thus, the manufacturing process quality, ensuring the uniformity of the material layers and interfaces, is a key factor.

Even assuming the uniform material layers and the ohmic contacts of the electrodes to the resistive layer, the position linearity and the resulting error of the position estimation using Formulas (1) and (2) worsen with an increase in the size of the light spot and the distance of its gravity center from the middle of the detector active area, depending on the shape and configuration of the electrodes on the resistive layer and the contribution of the series impedance to the total impedance of the detector. Nonlinear effects and corrections realizable by simple fast analog electronics are described in [21].

The position resolution of a PSD is the minimum detectable displacement of a light spot [7,9]. This means that it is related to the signal-to-noise ratio of the detector and read-out electronics. The position resolution can be assessed using the standard deviations $\overline{x_{\text{nPSD}}}$ and $\overline{y_{\text{nPSD}}}$ of the position coordinates X_{PSD} and Y_{PSD} , respectively (adapted with permission from Ref. [20]; copyright: 2022, SPIE):

$$\overline{x_{\text{nPSD}}} = 2k_X \frac{\sqrt{U_B^2 \overline{u_{nC}^2} + U_C^2 \overline{u_{nB}^2}}}{(U_B + U_C)^2} \quad (3)$$

$$\overline{y_{\text{nPSD}}} = 2k_Y \frac{\sqrt{U_A^2 \overline{u_{nD}^2} + U_D^2 \overline{u_{nA}^2}}}{(U_A + U_D)^2} \quad (4)$$

where $\overline{u_{nA}}$, $\overline{u_{nB}}$, $\overline{u_{nC}}$, and $\overline{u_{nD}}$ are the root-mean-square (rms) noises at the respective channel outputs. It is assumed that the noises from the individual channels are uncorrelated with each other.

2. Chip Construction and Assembly

A (100)-oriented $\text{Hg}_{1-x}\text{Cd}_x\text{Te}$ heterostructure, containing a lightly doped p^- -type narrow-gap absorber with the material composition $x = 0.2$, optimized for position detection of the 10–11 μm radiation at 205 K and sandwiched between wide-gap heavily doped contact layers [22], was grown by metalorganic chemical vapor deposition (MOCVD) on a CdTe-buffered semi-insulating (100) GaAs substrate. The structure was doped with iodine and arsenic as well-behaved and stable donor and acceptor dopants, respectively, by in situ incorporation during growth. The absorber thickness was reduced to about 2 μm in order to increase the differential impedance of this large LWIR photodiode. The input radiation beam essentially passed twice through the absorber, due to the internal reflection from the top of the detector mesa structure, covered with the indium electrode.

Chips of the TL-PSD devices were fabricated, flip-chip-bonded to sapphire carriers, mounted on a Peltier cooler, wired with thin gold leads to output pins, sealed in hermetic packages, integrated with read-out electronics, and scanned with a radiation spot. The chip-level layout used is shown in Figures 2–4. Figure 2b provides a top-view micrograph of the fabricated chip. The direction of illumination is indicated in Figure 3. Table 1 schematically presents a diagram of the layers in the mesa structure, with their donor N_D and acceptor N_A doping concentrations, compositions, and thicknesses, in more detail than in the drawings. In the first column, n^+ and p^+ denote donor and acceptor, respectively, heavy doping in a narrow-gap HgCdTe; N^+ and P^+ denote donor and acceptor, respectively, heavy doping in a wide-gap HgCdTe; p^- denotes acceptor light doping of the narrow-gap absorber. The net doping $N_A = 2 \times 10^{15} \text{ cm}^{-3}$ of the absorber is a result of subtraction of the background donor doping—ca. $8 \times 10^{14} \text{ cm}^{-3}$ —from the actual arsenic concentration. The wide-gap layers, N^+ -contact for electrons—and P^+ -contact for holes—are interfaced to the absorber through the graded-gap HgCdTe layers. The CdTe passivation at the edge of the mesa is deposited by sputtering.

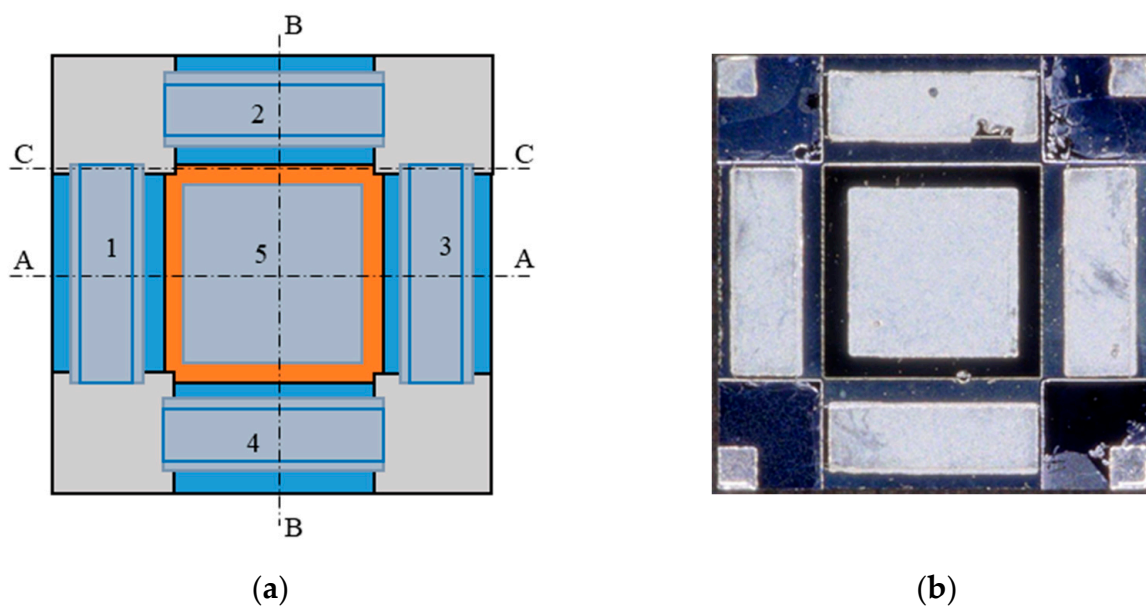


Figure 2. TL-PSD chip—top view: (a) a schematic drawing: 1, 2, 3, and 4 denote indium cathode electrodes, and 5 denotes an indium anode electrode; cross-sections A–A, B–B, and C–C are shown in Figures 3 and 4; (b) a micrograph of the fabricated chip.

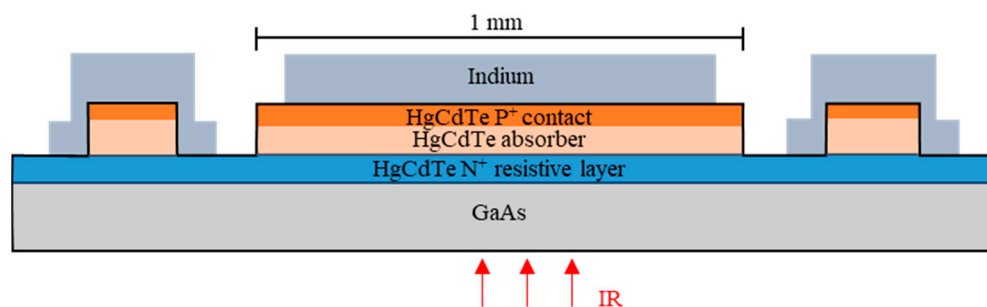


Figure 3. TL-PSD chip—the A–A and B–B cross-section, according to Figure 2.

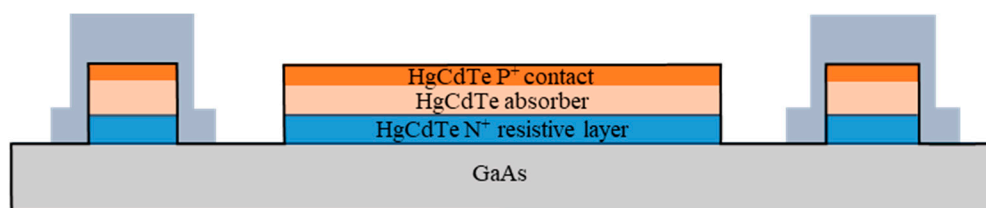
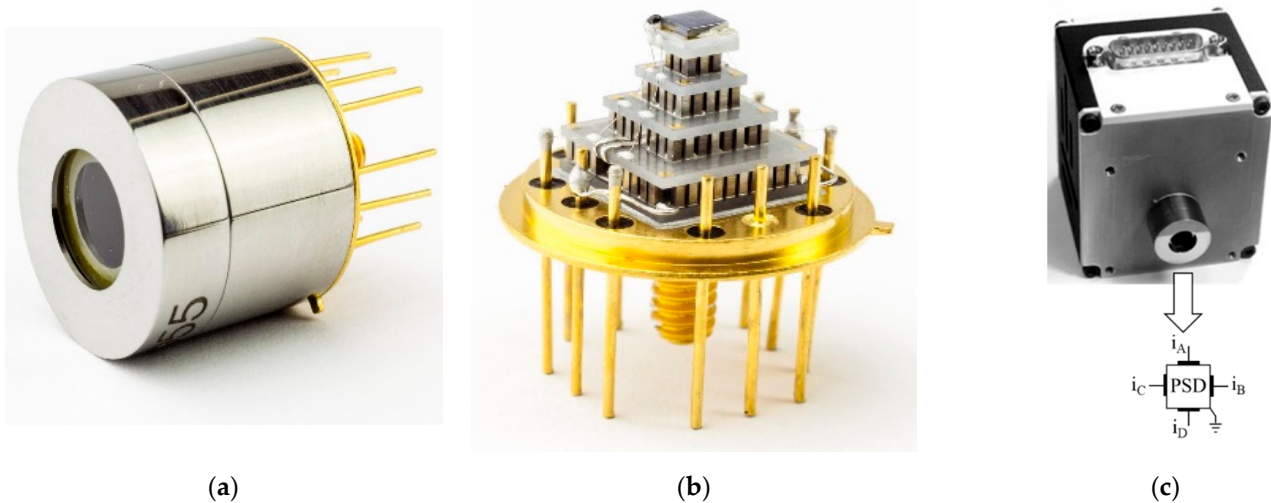


Figure 4. TL-PSD chip—the C–C cross-section, according to Figure 2.

The photographs in Figure 5 present the hermetically sealed detector package (Figure 5a); its inner parts (Figure 5b) with the TL-PSD dice, which is flip-chip indium bump bonded to the chip carrier, on the cooler cold finger, where the cooler is soldered to a TO8 header; and the detector shortly connected to the electronics package (Figure 5c).

Table 1. Schematic diagram of the layers in the mesa structure: their doping concentration, material composition, and thickness.

	-	-	Indium	>6.0 μm	
CdTe—passivation	n^+	$N_D = 3 \times 10^{17} \text{ cm}^{-3}$	$\text{Hg}_{0.88}\text{Cd}_{0.12}\text{Te}$	1.5 μm	CdTe—passivation
	p^+	$N_A = 5 \times 10^{17} \text{ cm}^{-3}$	$\text{Hg}_{0.85}\text{Cd}_{0.15}\text{Te}$	0.7 μm	
	P^+	$N_A = 5 \times 10^{17} \text{ cm}^{-3}$	$\text{Hg}_{0.65}\text{Cd}_{0.35}\text{Te}$	0.8 μm	
	Graded bandgap	Doping gradient	$\text{Hg}_{1-x}\text{Cd}_x\text{Te}$	1.1 μm	
	p^- -absorber	$N_A = 2 \times 10^{15} \text{ cm}^{-3}$	$\text{Hg}_{0.80}\text{Cd}_{0.20}\text{Te}$	2.0 μm	
	Graded bandgap	Unintentional doping	$\text{Hg}_{1-x}\text{Cd}_x\text{Te}$	1.6 μm	
	N^+	$N_D = 3 \times 10^{17} \text{ cm}^{-3}$	$\text{Hg}_{0.68}\text{Cd}_{0.32}\text{Te}$	4.6 μm	
	Buffer	Unintentional doping	CdTe	2.7 μm	
	Substrate	semi-insulating	GaAs	400 μm	

**Figure 5.** Detector package (adapted with permission from Ref. [20]; copyright: 2022, SPIE): (a) the hermetic housing of the TL-PSD chip; (b) the TL-PSD chip on the four-stage Peltier cooler cold finger; (c) the TL-PSD detector integrated with the electronics package, and a spatial orientation of the cathode electrodes of the signal channels A, B, C, and D is also shown.

3. Dark Current Sources

Unfortunately, the radiative generation from the 300 K background is negligible compared to the non-radiative G-R components in this device. The dark current is suppressed with cooling, and the reverse bias further reduces the carrier concentrations below their thermal equilibrium levels thanks to a phenomenon specific to infrared narrow-gap semiconductor detectors—suppression of the Auger generation by extraction and exclusion of electric charge carriers with the reverse bias [23].

The dark current sources relevant to this detector are as follows [4] (pp. 247–260), [24] (pp. 82–86):

- Diffusion currents from the quasi-neutral (neutral) regions, mainly from the depleted in carriers but still neutral absorber volume, with their thermal G-R components:
 - Auger 7 and Auger 1; in HgCdTe, the former dominates over the latter if the concentration of holes is more than about 10 times greater than that of electrons [24] (pp. 34, 136, 137), [25] (pp. 83–85);
 - Shockley–Read–Hall (SRH);
- Currents from the space-charge (depletion) regions around (metallurgical) junctions:

- SRH (thermal G-R current in the space-charge region [26]);
- Trap-assisted tunneling (TAT) [27,28], with nearly linear dependence on reverse bias voltage < 1 V;
- Band-to-band tunneling (BTB), with voltage-dependence much stronger than linear;
- Possible components associated with injection to the absorber from the contact regions, mainly over the P⁺ barrier;
- Surface generation: SRH, tunneling, and conduction channels:
 - at the edge of the mesa;
 - along dislocations intercepting the junctions [29,30], i.e., reaching the space-charge regions in the absorber interfaces;
- Photoelectric gain mechanisms, affecting the dark current, noise, and responsivity but not the detectivity (sensitivity) of the detector [31,32];
- Internal radiative G-R is not important due to the photon recycling [33].

4. Noise Sources

The detector current fluctuates and so generates noise. Four types of noise are of importance in semiconductors [34]:

- Thermal (Johnson) noise and shot noise, with a constant (white) spectral density within the noise equivalent bandwidth;
- Random telegraph noise—a noise type that presents as a binary fluctuation in dark current, with a Lorentzian-shaped noise spectral density;
- 1/f noise, with the inverse dependence of the noise spectral power on frequency:

$$\overline{i_{n1/f}^2(f)} = \overline{i_{n1/f}^2(1 \text{ Hz})} / f^\gamma \quad (5)$$

where $\overline{i_{n1/f}}$ is the 1/f noise component of the root-mean-square (rms) noise current spectral density, f is the frequency, and $\gamma = 1.0 \pm 0.1$ in a wide frequency range, after [34]. This is the dominant type of noise in our PSD.

Scientists agree that 1/f noise in semiconductor devices is caused by fluctuations in electrical conductivity but differ on whether carrier concentration fluctuations [35] (pp. 207–228) or carrier mobility fluctuations [34], or both [36–39], are the cause.

The first paper on 1/f noise in HgCdTe photodiodes was published by Tobin et al. [40] in 1980. The authors found the 1/f noise to be proportional to the surface generation and surface leakage current of implanted n⁺-p MWIR HgCdTe photodiodes for a wide range of operating temperatures, from cryogenic with domination of the surface generation and surface leakage to higher temperatures, where the diffusion dark currents prevailed. The coefficient of proportionality, α , is often referred to as the Tobin coefficient:

$$\alpha = \frac{\overline{i_{n1/f}(f, T_d, V_b)} \times \sqrt{f}}{i(T_d, V_b)} = \frac{\overline{i_{n1/f}(1 \text{ Hz}, T_d, V_b)}}{i(T_d, V_b)} \quad (6)$$

where i is the detector overall current or one of its components, T_d is the detector operating temperature, and V_b is the detector bias voltage. According to Tobin et al., the surface generation and surface leakage could be modulated by fluctuations in the surface potential, thus generating the 1/f noise. The authors were inspired by numerous works on 1/f noise studied in silicon and germanium filaments, p-n junctions [41], and MOS transistors, including McWhorter's suggestion in 1953 that variations in the occupancy of the slow surface states caused conductivity fluctuations of semiconductor filaments and had a wide uniform spectrum of relaxation times corresponding to the 1/f noise [35] (pp. 207–228). Single-electron slow trapping de-trapping generates random telegraph noise [42]. In photodiodes, the slow trapping events mainly occur in passivation near the semiconductor surface or in the dislocations intercepting the junction, both in depletion regions.

Exemplary $1/f$ noise calculations for HgCdTe photodiodes were performed, based on McWhorter's theory [29,43–45] or taking into account carrier mobility/scattering fluctuations [38,46]. The dislocations intercepting the junction were found to induce TAT and $1/f$ noise and are supposed to cause bandgap narrowing and getter impurities that can act as active trap centers [30,32,38,42,46–48].

In 2019, the new, more demanding standard was introduced by Teledyne—the MWIR and LWIR HgCdTe reverse biased photodiodes with fully depleted absorbers and close to the 300 K background limited performance [49]. In the fully depleted absorber, dislocations can be inactivated (“frozen”) because of lack of carriers throughout the absorber, even at the highest reported [49] operating temperature of 250 K, as they have been depleted and inactivated so far using cryogenic cooling. Then, the $1/f$ noise can be greatly reduced, providing the heteropassivation is applied by interdiffusion between the HgCdTe and the CdTe passivation layer during the high-temperature annealing. High-temperature annealing was also found to inactivate defects and dislocations in the active volume of the detector [47].

Another way to avoid or significantly reduce the $1/f$ noise is to minimize the depletion area using photodiodes optimized for 0 V bias or biased barrier devices, such as nBn [50,51].

5. Parameters of the Detector's Equivalent Circuit

The equivalent circuits treat the TL-PSD like a four-way output current divider with four resistances. Their values can be approximated using the formulas written in Figure 6. The least error of such approximation is obtained at the center position of the light spot, with the radiation distribution approximated by Dirac's delta function. Figure 7 shows a piece of the equivalent circuit suited for the finite element analysis—two adjacent cells of an array consisting of $n \times n$ equal cells. R_p denotes the differential parallel resistance and C_p denotes the differential parallel capacitance of the photodiode at a given reverse bias. The R_{sh} series resistance is the square sheet resistance of the resistive layer, and $R_{s,com}$ is the common series resistance, which is approximately the series resistance of the photodiode excluding the resistive layer. Both models are limited to the small signal case for which the input radiation power and the photocurrent are within the detector linear operation range.

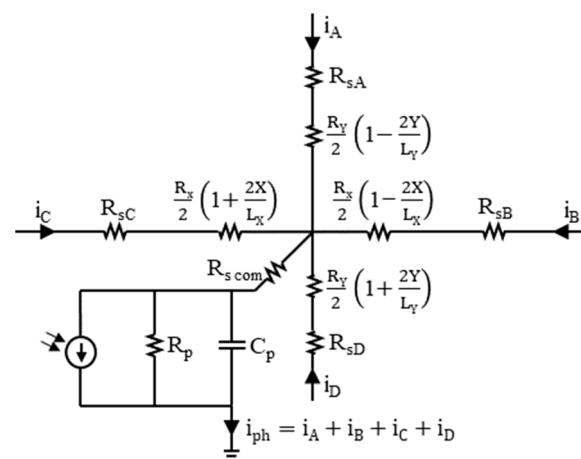


Figure 6. TL-PSD equivalent circuit with the approximated formulas for the resistances of the photocurrent divider in the resistive layer, related to the light spot position (X, Y) , where $(0, 0)$ is in the center of the photosensitive area. The following values were determined at the detector operating temperature $T_d = 205$ K and reverse bias $V_b \approx 0.16$ V: $R_p \geq 100$ Ω ; $C_p \approx 1$ nF; $R_{s,com} \approx 0.6$ Ω —the lead wire resistance; R_X and R_Y may be assumed to equal $R_{sh} = 5.5$ Ω —the measured sheet resistance of the resistive layer; $R_{sA} = 8.9$ Ω , $R_{sB} = 8.9$ Ω , $R_{sC} = 9.0$ Ω , and $R_{sD} = 9.2$ Ω , with the main contribution of 8 Ω of the preamplifier input impedance, later calculated using Equation (9), and with minor contributions of contact resistance values from Table 2 and 0.6 Ω of the lead wire resistance.

Table 2. Differential resistance between the opposite cathode electrodes at ± 16 mA, based on the results shown in Figure 9, at $T_d = 205$ K.

	R, Ω	$\Delta R = R - R_{sh}, \Omega$	$\Delta R/R_{sh} = R/R_{sh} - 1$
R_{sh}	5.5	0.00	0.0%
$R_{C-B} (-109 \text{ mV}, -16 \text{ mA})$	5.8	0.28	5.1%
$R_{C-B} (+109 \text{ mV}, +16 \text{ mA})$	5.8	0.35	6.3%
$R_{D-A} (-109 \text{ mV}, -16 \text{ mA})$	5.8	0.30	5.4%
$R_{D-A} (+117 \text{ mV}, +16 \text{ mA})$	6.1	0.63	11.5%

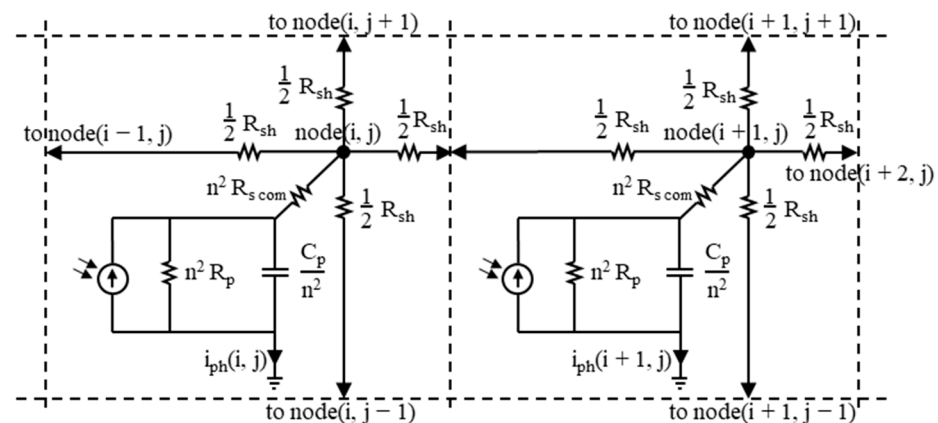


Figure 7. Two cells of the TL-PSD equivalent circuit suited for the finite element analysis. The following values were determined at $T_d = 205$ K and $V_b \approx 0.16$ V: $R_p \geq 100 \Omega$; $C_p \approx 1$ nF; $R_{sh} = 5.5 \Omega$ —the resistive layer sheet resistance; $R_{s,com} = 0.6 \Omega$ —the lead wire resistance.

The linearity of the PSD signal versus the input radiation power as well as versus the light spot position and the resolution of the position measurement improve when the differential parallel impedance $R_p || C_p$ becomes much greater than the series impedance. The resistance of the photodiode was determined from DC measurement of its I-V characteristics, plotted in Figure 8, at the detector operating temperature $T_d = 205$ K. It was important that the measurement was performed with all the A, B, C, and D outputs connected together. A significantly different shape of the characteristics, with an increased contribution of the series resistance, would be obtained if, for example, only one channel was connected to the ammeter and the other three were open.

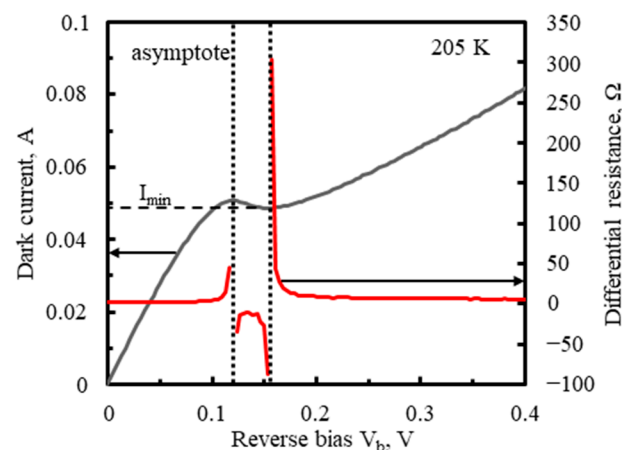


Figure 8. Dark I–V characteristics of the TL–PSD photodiode with the 10–11 μm long wavelength cut-off at $T_d = 205$ K.

At the reverse bias V_b outside the range of 0.1–0.2 V, the detector resistance dropped below $<1 \Omega$ and was dominated by the series resistance. With V_b increase to 0.12 V, the dark current became saturated due to the suppression of Auger generation, before the loss of T_d stabilization by too much Joule heating could occur. The dark current slightly decreased with V_b in the range where the differential resistance was negative and then increased due to TAT, which narrowed the range of high differential resistances to a few millivolts of V_b . Even infinite differential resistance is theoretically possible, but a maximum of just over 100 Ω has been reached. This was due to the narrow V_b range with high differential resistances and the preamplifier input offset voltage, ranging from -0.5 to 0.5 mV [52].

The suppression of Auger generation with reverse bias is possible with low doping of the relatively thin HgCdTe absorber layer. However, in spite of its light p^- -type doping (Table 1) and small thickness, we did not manage to suppress the electron concentration in the absorber to a negligible value. The minimal dark current at $V_b \approx 0.16$ V occurred at the level corresponding to the Auger 1 rather than the Auger 7 diffusion current and was close to that predicted by “Rule 07” [53], a metric derived in 2007 for detectors limited by diffusion currents generated in a HgCdTe n-type absorber with extrinsic donor doping 10^{15} cm^{-3} . Nevertheless, “Rule 07” has become a popular benchmark for state-of-the-art IR photodetectors based on other technologies, such as nBn and type II strained-layer superlattices.

The surface at the edge of this mesa structure insignificantly contributes to the dark current generation, due to the mesa transverse size being > 100 times greater than the carrier diffusion length. This was confirmed in dark current measurements of photodiodes of variable size from the same wafer. Nevertheless, the surface generation may significantly contribute to $1/f$ noise, as in [54].

The R_{sh} sheet resistance was checked as the resistance R_{C-B} between the opposite cathode electrodes C and B and as the resistance R_{D-A} between the opposite cathode electrodes D and A, when the anode electrode was electrically open. Figure 9 plots the differential resistances R_{C-B} and R_{D-A} and the currents versus the voltage put between the electrodes. The minimum R_{C-B} and R_{D-A} values were around 0 V and amounted to 5.5 Ω and 5.7 Ω , respectively, close to 5.5 Ω of the R_{sh} measured on the wafer before chip-processing. Assume an even distribution of the dark current I_d between the cathode electrodes, $I_{d/ch} = 12$ mA per one channel using 0.16 V of the reverse bias. During a normal operation of the PSD, when the photosignal varies linearly with the input radiation power, the amplitude of the total photocurrent i_{ph} does not exceed 4 mA, i.e., 1 mA per channel. The R_{C-B} and R_{D-A} values for ± 16 mA, corresponding to the sum of ± 12 mA of the dark current and ± 4 mA of the photocurrent, are given in Table 2.

The resistance characteristics, exhibiting some nonlinearity and asymmetry, and the observed differences between the R_{C-B} , R_{D-A} , and R_{sh} values indicate the possible contribution of the resistance of the metallization contact to the resistive layer. This is comparable to the resistance 0.6 Ω of the 25 μm diameter, 1 cm long gold lead wire and its compression bond used to connect the cathode electrode with the output pin. The sum of the metal–semiconductor contact resistance and that of the lead wire makes about 1 Ω of the detector series resistance at the output of each channel. It does not change with the light spot position and negatively affects the position error and the PSD linearity. Unfortunately, it was small compared to the 8 Ω for the input impedance of the integrating preamplifier, calculated later using Equation (9).

The inductance of the single lead wire can be assumed to be $L = 13.3$ nH, as the inductance of a straight gold wire 25 μm in diameter and 1 cm long [55,56]. For the applied integration times, which are time intervals τ_{CDS} of the correlated double sampling (CDS; Section 6), $\tau_{CDS1} = 1$ μs and $\tau_{CDS2} = 0.5$ μs , the 3 dB frequencies f of an integrating preamplifier transfer function are those of $\text{sinc}(\pi \tau_{CDS} f)$ —the Fourier transform of a rectangular pulse of τ_{CDS} width— $f_{3dB1} = 0.44/\tau_{CDS1} = 440$ kHz and $f_{3dB2} = 0.44/\tau_{CDS2} = 880$ kHz, respectively [57]. The impedance modules $|Z_L|$ of the wire introduced by the inductance L at

$f = f_{3dB1}$ and $f = f_{3dB2}$ are $|Z_{L1}| = 2\pi \times f_{3dB1} \times L = 0.036 \Omega$ and $|Z_{L2}| = 2\pi \times f_{3dB2} \times L = 0.072 \Omega$, negligible in comparison with 0.6Ω of the wire resistance.

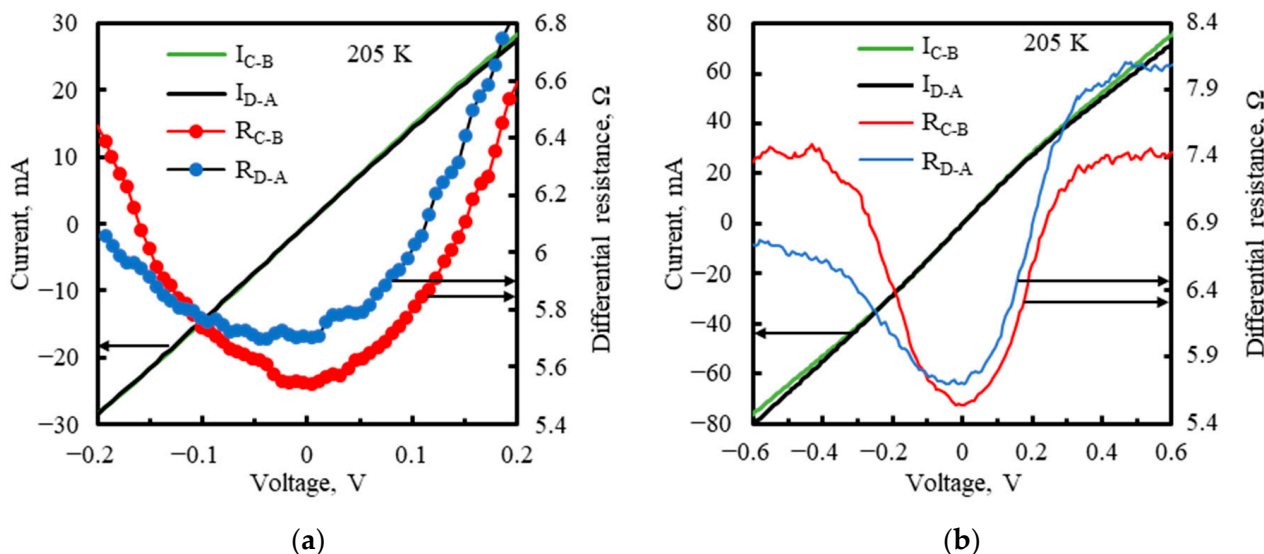


Figure 9. Current and differential resistance versus voltage between the opposite cathode electrodes. The DC measurement at $T_d = 205$ K with the photodiode electrically open. R_{C-B} denotes resistance between the electrodes C and B, and R_{D-A} denotes resistance between the electrodes D and A. These are resistances measured between the respective output pins outside the PSD hermetic package minus the resistance 1.2Ω of two thin $25 \mu\text{m}$ diameter golden lead wires, connecting the output pins with the cathode electrodes. (a) Results shown in the bias voltage range -0.2 V to $+0.2$ V. (b) The same, with added results in the greater bias range.

The $R_{s\text{ com}}$ common series resistance 0.6Ω was introduced by the $25 \mu\text{m}$ diameter, 1 cm long gold lead wire and its compression bond used to connect the anode electrode with the output pin.

The parallel capacitance C_p scales proportionally to the photodiode photosensitive area and was only estimated from measurements of some reverse biased photodiodes, much smaller than the PSD photodiode and made of wafers similar to those used for this PSD. These were time response measurements using fast-decay laser pulses [22,58,59] as well as small-signal reflectance measurements with the vector network analyzer [60]. The C_p was estimated to be ca. 1 nF. As for R_p , such a value for C_p was possible due to suppression of the Auger generation with the reverse bias.

The photocurrent i_{ph} at the anode electrode (Figures 6 and 7) is the sum of the photocurrents from all the four cathode electrodes. It can be found for a given input radiation spectral power $P_{in\lambda}$ and a given spectral current responsivity $R_{i\lambda}$ of the detector using the relation: $i_{ph} = P_{in\lambda} \times R_{i\lambda}$. The low frequency $R_{i\lambda}$ of the PSD photodiode is shown in Figure 10. It was measured with a Fourier transform infrared spectrometer calibrated with a black-body radiation source with an accuracy of $\pm 20\%$. Short-wavelength radiation is largely filtered by the wide-gap cathode resistive layer, through which radiation enters the absorber, while the long-wavelength tail of the spectral characteristics is determined by the width and composition of the narrow-gap absorber.

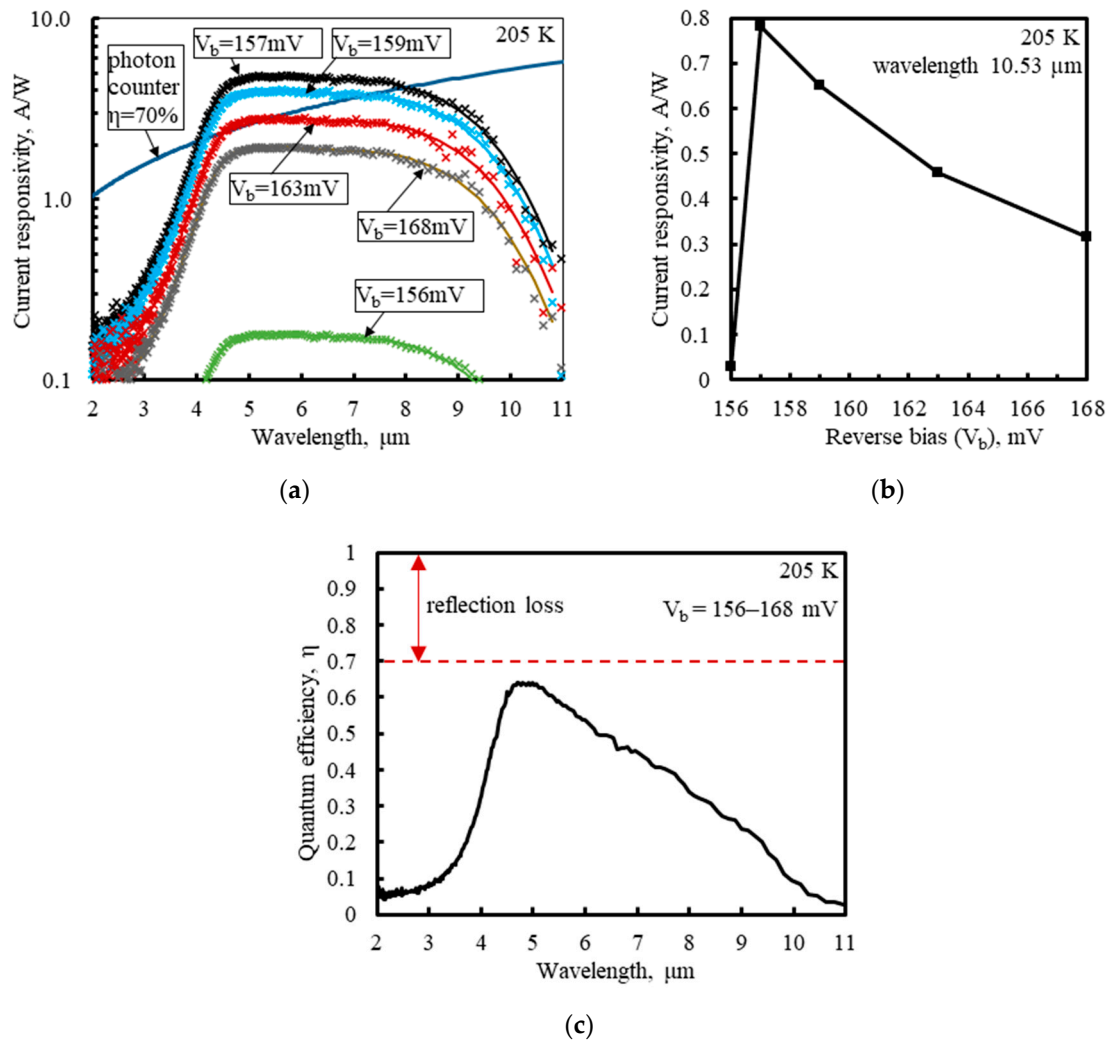


Figure 10. Spectral responsivity of the PSD photodiode at $T_d = 205$ K, from the photocurrent at the anode common contact, measured with the Fourier transform infrared spectrometer for the various reverse bias voltages V_b : (a) spectral characteristics (adapted with permission from Ref. [20]; copyright: 2022, SPIE); (b) rapid change in the responsivity with V_b around 0.16 V; (c) spectral quantum efficiency $\eta = \eta_r \times \eta_a$.

Figure 10 reveals a strong dependence of the responsivity magnitude on V_b around 0.16 V, in the range of the high differential resistances, presented in Figure 8. The responsivity, strongly limited by the series resistance, was boosted with V_b between 156 mV and 157 mV and then gradually decreased as V_b increased. The rise in the responsivity was correlated with the sharp increase in the differential resistance of the detector, where the parallel resistance R_p was enhanced in relation to the series resistance. Moreover, at V_b in the range of 157 mV to 163 mV, the spectral responsivity exceeded that of the ideal photon counter with the quantum efficiency 70%, conforming to $100\% - 70\% = 30\%$ of the radiation reflection losses in the detector, mainly at the air-GaAs interface of the chip substrate. This was the evidence of the photoelectric gain g_{ph} greater than unity. The g_{ph} value was estimated to equal ca. 1.7 for $V_b = 159$ –160 mV, based on the following formula:

$$g_{ph} = \frac{R_{i\lambda}}{e\eta_r\eta_a / (h\frac{c}{\lambda})} \quad (7)$$

where h is Planck's constant, c is the speed of light in a vacuum, $(h\frac{c}{\lambda})$ is the photon energy, η_a is the absorption quantum efficiency deduced from fitting of modeling of the

infrared absorption and transmission to the measured relative spectral response of the detector and room-temperature transmission of wafers with HgCdTe layers [61], $\eta_r = 70\%$ is the quantum efficiency related to the radiation reflection losses, and e is the charge of the electron.

6. Pulsed Radiation Measurement

The read-out circuitry (ROC) for the pulsed radiation measurements was realized in the form of a switched integrating transimpedance operational amplifier (op-amp) at each of the PSD's four outputs. Figure 11 presents a general scheme of the ROC. The integrating op-amp consisted of the fast SiGe-based bipolar input ADA4896 op-amp integrated circuit chip [52], characterized by a low input current and voltage noise density, and the integrating capacitor $C_i = 220$ pF in the op-amp negative feedback loop, thus providing conversion of the integrated photocurrent to the output voltage across the C_i .

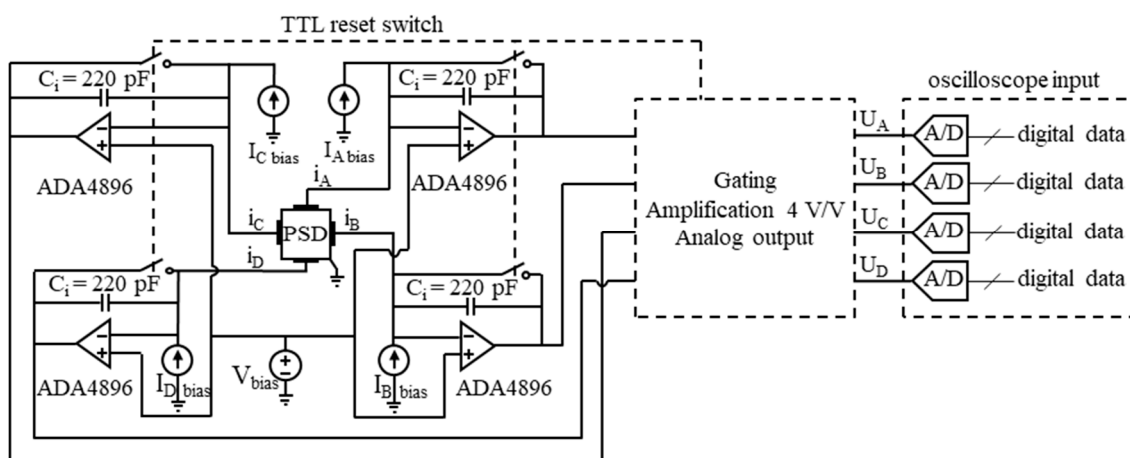


Figure 11. General scheme of the read-out electronic circuit suited to the PSD photodetector, with the switched integrating preamplifiers, current sources compensating the reverse bias current individually for each channel, and one voltage source ensuring the constant reverse bias voltage for all the four channels. The output voltage was measured with a sampling analog-to-digital converter of the oscilloscope input.

The applied integration intervals were synchronized with 100 ns pulses of input radiation, emitted from the quantum cascade laser (QCL) with the 10 kHz repetition frequency. The timing of integration and sampling of the output voltage was controlled by a TTL-voltage compatible switching. This is illustrated in Figure 12, where Figure 12a shows an example output voltage waveform from one channel with a ca. 0.95 V photoresponse to the 100 ns laser pulse and Figure 12b plots the output voltages from all four channels with the unlighted detector. Correlated double sampling (CDS) was applied. The first and second sample of each pair of the correlated samples of the output voltage were measured at time instants M1 and M2, respectively, when the reset switch (RS) was open. The first sample V_{M1} preceded the start of the radiation pulse and followed 0.5 μ s after opening the RS at 0 ns. The second sample V_{M2} was taken well after the end of the radiation pulse, when all the photocurrent had been integrated. The voltage V_{M1} was subtracted from the voltage V_{M2} . The measurement result was $V_{M2} - V_{M1}$, the CDS voltage. Next, the RS was closed for a time more than sufficient for discharge of the integrating capacitor. However, in the reset state (zeroing), the voltage across the capacitor settled at a level slightly different from zero. This zeroing offset could have been due to the op-amp input offset voltage, the flow of the uncompensated bias current through the RS, and charge injection during change of the RS state. The CDS dramatically reduced 1/f noise and the zeroing offset. The remaining output offset was due to the inaccurate compensation of the dark current, a small part of which flowed through the integrating capacitor.

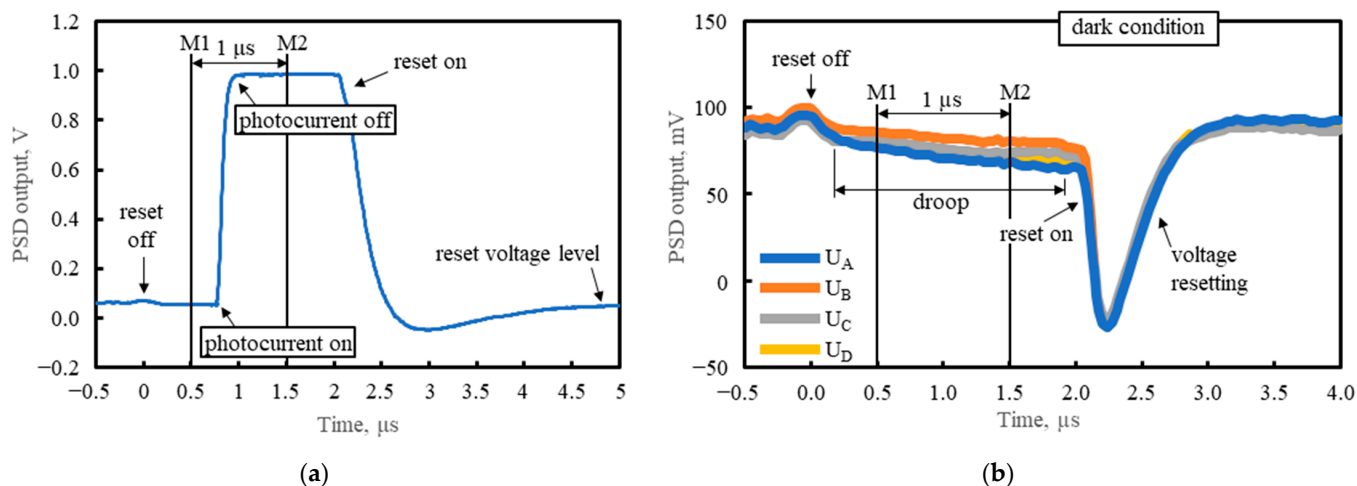


Figure 12. Reset-and-integrate timing with the sampling time instants M1 and M2 shown: (a) example waveform of the output voltage from one channel, when the detector was lighted with the 100 ns laser pulse; (b) waveforms of the output voltages from all the channels, A, B, C, and D, when the detector was shielded from radiation.

This switched (also called box-car) integration of a signal improves the signal-to-noise ratio and is the preferred method for measuring weak pulsed radiation if an increase in measurement time is tolerated, such as when measuring pulse energy.

The input impedance of the ROC should be minimized so as not to unduly limit the photocurrent and the linearity of the PSD. This was achieved with the fast transimpedance op-amps, characterized by the relatively high open loop gain crossover frequency. The impedance mismatch was not significant here due to the limited bandwidth imposed by the applied value of the integration time τ_{CDS} .

The ROC should ensure the constant reverse bias voltage across the photodiode along with compensation of its bias (dark) current. The bias voltage should be within a relatively narrow range (Figures 8 and 10), allowing sufficient depletion of carriers throughout the absorber, thus increasing the parallel impedance in relation to the series impedance so that the latter does not unreasonably limit the responsivity and linearity. The optimal bias voltage is then the same for all the channels. Its common regulation, as shown in Figure 11, was correct, as opposed to being separate for each channel.

Two detectors, each with a separate PSD chip from the same wafer, were assembled and integrated with the read-out electronics, forming two compact samples of PSD modules #1 and #2. The modules were attached to a heat-sink, which helped in the electronic stabilization of the detector operation temperature with a precision of 0.01 K. The output voltage was measured with an oscilloscope and mapped across the photosensitive area in a setup shown in Figure 13.

The laser beam was focused with a parabolic mirror onto the photosensitive area of the PSD. A motorized X-Y stage, actuated by stepper motors, enabled scanning of the photosensitive area with the radiation spot. The measurement was controlled by a script written in Python programming language, installed on a computer (PC). The script collected and organized the sampling data of the output voltages U_A , U_B , U_C , and U_D from all four channels, obtained from the oscilloscope, and the data of the actual (X, Y) position of the radiation spot on the photosensitive area, received from the encoders of the stepper motors through their controllers. The actuation of the stepper motors was synchronized by the script with the time the PC received data from the oscilloscope and the encoders. Based on the gathered data, the script calculated the beam spot position (X_{PSD} , Y_{PSD}) using Formulas (1) and (2), assigned it to the actual (X, Y) position data from the encoders, and presented the results in a graphical form.

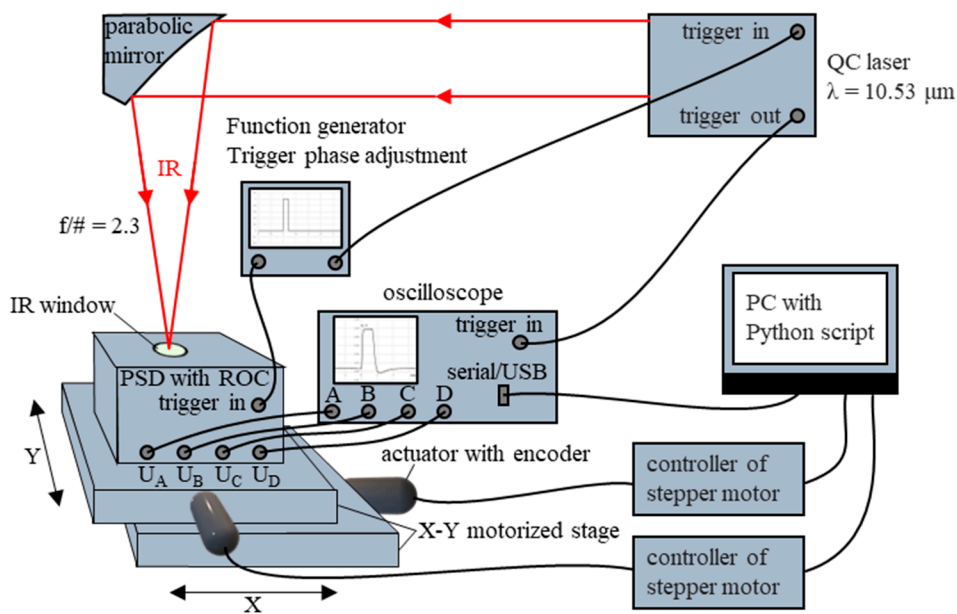


Figure 13. Measurement setup for mapping a PSD photosignal across the photosensitive area.

An example waveform of the output voltage together with the input radiation power from the pulsed laser is presented in Figure 14. The radiation power was measured using another, uncooled photovoltaic detector type PVM-10.6-4×4, manufactured by VIGO Photonics S.A. (VIGO) (Ożarów Mazowiecki, Poland) [16,17,62], with the HgCdTe heterostructure consisting of multiple photovoltaic junctions connected in series that are distributed over a large photosensitive area of 4 mm × 4 mm. The PVM-10.6-4×4 detector is characterized by a large linearity range of the input radiation power and a low time constant of 1.0–1.5 ns, compared to the PSD presented herein.

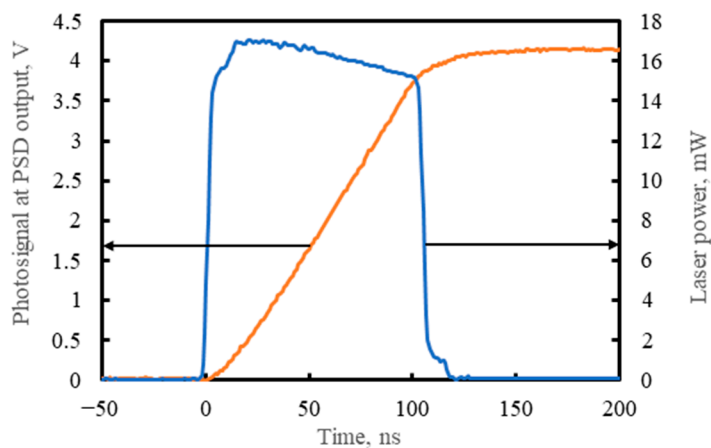


Figure 14. Example waveforms: the input power of QCL radiation focused centrally on the PSD photosensitive area and the voltage signal from one of the PSD module outputs (adapted with permission from Ref. [20]; copyright: 2022, SPIE).

Based on the PSD equivalent circuit from Figure 7 and the values of its elements given therein, the time constant τ_{PSD} of the single-channel photoresponse can be approximated as follows:

$$\tau_{\text{PSD}} = [R_p \parallel (2 \times R_{\text{scom}} + 0.5 \times R_{\text{sh}} + Z_{\text{in amp}})] \times C_p \approx (2 \times R_{\text{scom}} + 0.5 \times R_{\text{sh}} + R_{\text{in amp}}) \times C_p = (1.2 \Omega + 0.5 \times 5.5 \Omega + 8 \Omega) \times 1 \text{ nF} = 12 \text{ ns} \quad (8)$$

where the detector is loaded by the integrating preamplifier input impedance $Z_{in\ amp}$ (Figure 11), which in fact is the resistance $R_{in\ amp}$ for the considered frequencies $> 100\text{ kHz}$ and can be calculated as follows:

$$Z_{in\ amp} = R_{in\ amp} = (2\pi C_i f_c)^{-1} = (2\pi \times 220\text{ pF} \times 90\text{ MHz})^{-1} = 8\ \Omega \quad (9)$$

where f_c is the open loop gain crossover frequency of the ADA4896 op-amp used [52].

As was expected, neither the PSD nor the preamplifier input contributed significantly to the time of the PSD response to the 100 ns laser pulse (Figure 14).

Figure 15 demonstrates the characteristics of the signal from the PSD module output $U_{out} = U_A \approx U_B \approx U_C \approx U_D$ versus the energy of the radiation pulse of width $t_{pulse} = 100\text{ ns}$ and shows the linear operation limit equal to $U_{out,3\%dev}(t_{pulse} = 100\text{ ns}) = 1.5\text{ V}$ at a 3% drop from the linear response. This corresponds to $0.54\text{ nJ} \pm 20\%$ of the single-pulse energy at center illumination, where the signals from each channel are approximately equal, within $\pm 10\%$ of the average. With deviation from center illumination, the pulse energy corresponding to the linear operation limit decreases to compensate for the increasing signal at the output with the highest voltage. The energy of the radiation pulse was measured by integrating the radiation power waveform obtained with the VIGO PVM-10.6-4 \times 4 detector (Figure 14).

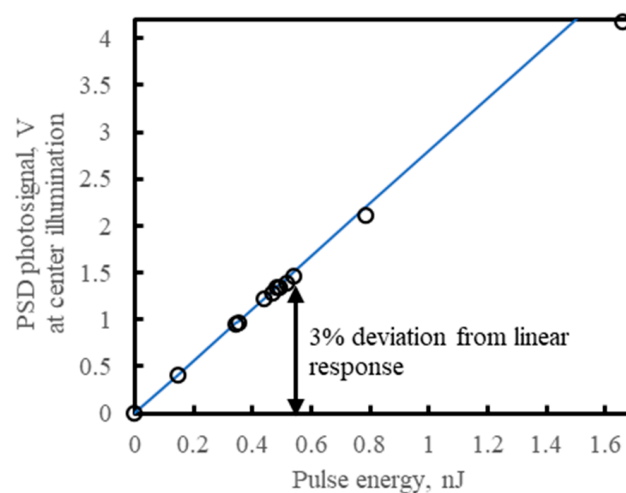


Figure 15. Linearity characteristics—the PSD module output signal versus the energy of the single radiation pulse at center illumination, similar for the samples #1 and #2 of the PSD modules. Averaging no. 64. The QCL 100 ns pulses $\lambda = 10.53\ \mu\text{m}$, the repetition rate 10 kHz, the Gaussian-like radiation spot of the $1/e^2$ diameter $240\ \mu\text{m}$, $\tau_{CDS} = 1\ \mu\text{s}$. The PSD photodiode was operated at $T_d = 205\text{ K}$ and the reverse bias $V_b = 0.16\text{ V}$.

It is optimal to operate within and not too far from the detector's linear operation limit. Exceeding this limit could lower the differential impedance of the detector, the high value of which is crucial for good performance and stable operation. However, assume this PSD operates at the signal close to its linear operation limit, at a 3% drop from the linear response. Then, the photocurrent per channel $I_{ph/ch,3\%dev} = 0.8\text{ mA}$:

$$I_{ph/ch,3\%dev} = U_{out,3\%dev} \times C_i / K_u / t_{pulse} = 1.5\text{ V} \times 220\text{ pF} / 4 / 100\text{ ns} = 0.8\text{ mA} \quad (10)$$

where $K_u = 4\text{ V/V}$ is the gain of the output stage of the preamplifier (Figure 11). This photocurrent puts a significant voltage $U_{s,3\%dev} = I_{ph/ch,3\%dev} \times R_s = 10\text{ mV}$ across the series resistance $R_s = 2 \times R_{scom} + 0.5 \times R_{sh} + R_{in\ amp} = 1.2\ \Omega + 0.5 \times 5.5\ \Omega + 8\ \Omega = 12\ \Omega$, from Equation (8), thus reducing by 10 mV the reverse bias voltage across the absorber and its interfaces. With a constant input radiation power, the photocurrent and photovoltage put across the series resistance of the corresponding channel increase with the distance of

the radiation beam from the central illumination point. Thus, the reverse bias voltage, if set to optimal for central illumination, will be less than optimal the farther the radiation beam is moved away from the center. This also reduces the detector resistance in relation to the series resistance, lowers the responsivity and adds to the position nonlinearity.

The PSD area was scanned with 100 ns pulses of QCL radiation of $\lambda = 10.53 \mu\text{m}$ and energy of 0.26 nJ, focused on a spot with a Gaussian-like profile (Figure 16) of the $1/e^2$ diameter $240 \mu\text{m}$, with a repetition rate of 10 kHz. The PSD was operated at 205 K, and the reverse bias voltage $V_b = 0.16 \text{ V}$, using $\tau_{\text{CDS}} = 1 \mu\text{s}$. The resulting signal chromatic maps of the photosensitive area are presented in Figures 17–19. The scan results in Figures 20 and 21 were obtained under the same conditions.

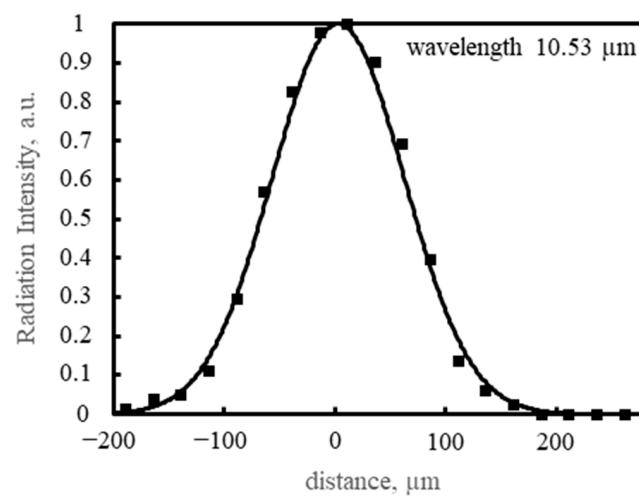


Figure 16. Gaussian-like profile of a radiation spot emitted by the QCL. The $1/e^2$ diameter is $240 \mu\text{m}$, measured with another Peltier-cooled HgCdTe photodiode with a small $30 \mu\text{m} \times 30 \mu\text{m}$ photosensitive area, type PV-3TE-10.6-0.03 \times 0.03, manufactured by VIGO Photonics S.A.

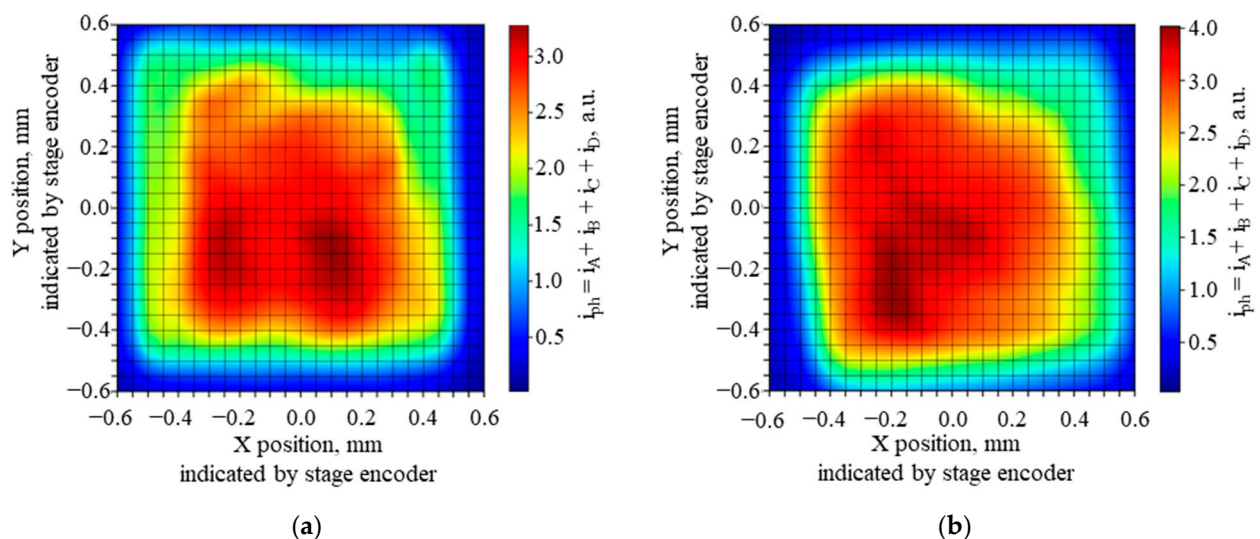


Figure 17. Chromatic map of the sum of the signals from the channels A, B, C, and D for two samples of the PSD modules: (a) sample #1; (b) sample #2. Averaging no. 32. The maximal signal from a single channel was 1.2 V.

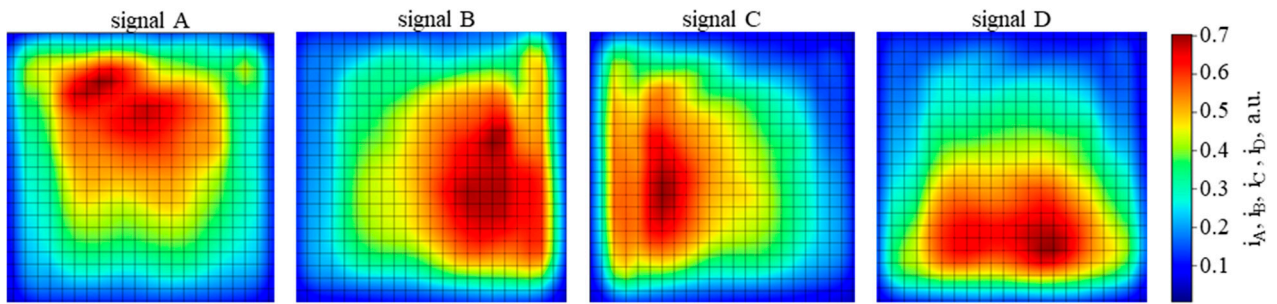


Figure 18. Signal chromatic maps of the photosensitive area of the PSD module sample #1, taken from the individual channels separately. Averaging no. 32. The maximal signal 1.2 V.

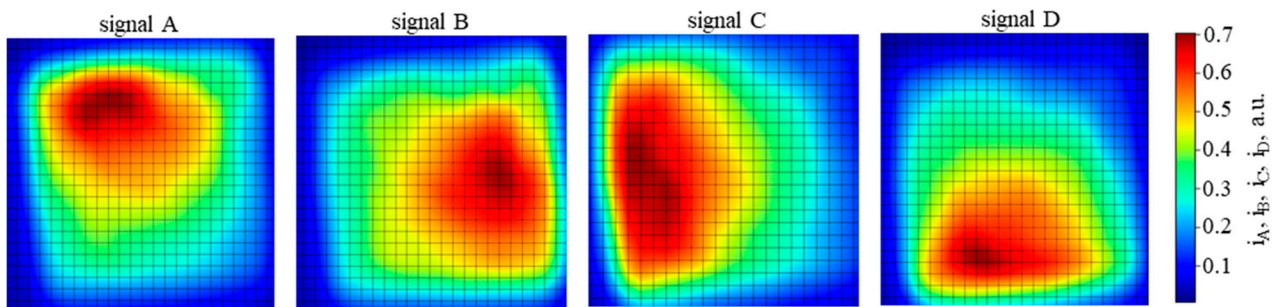
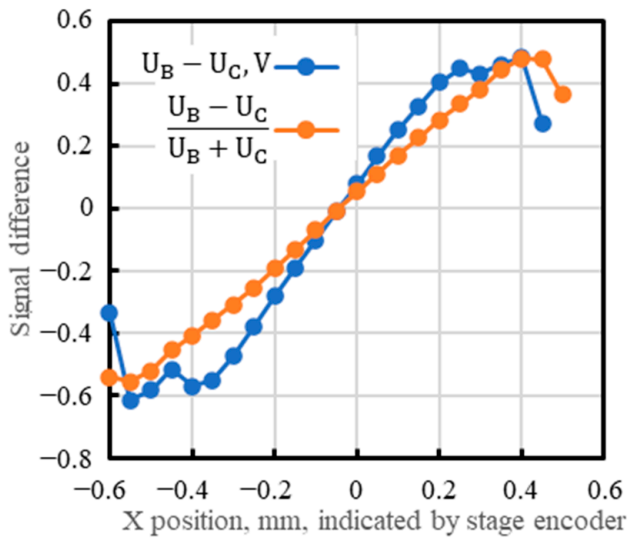
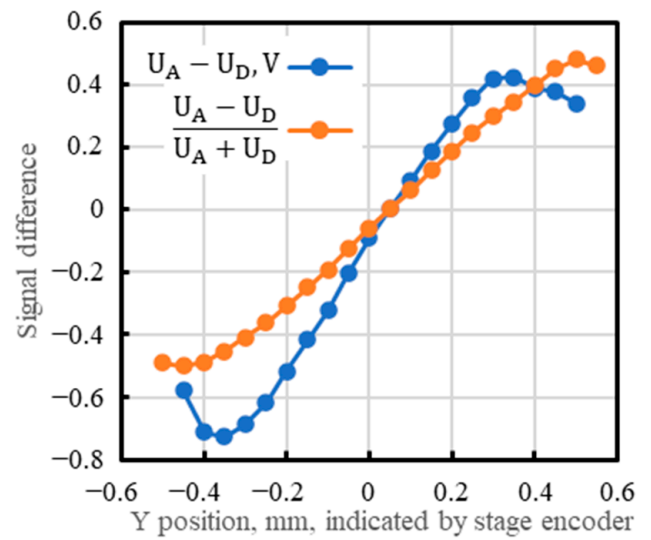


Figure 19. Signal chromatic maps of the photosensitive area of the PSD module sample #2, taken from the individual channels separately. Averaging no. 32. The maximal signal 1.2 V.



(a)



(b)

Figure 20. Difference between signals from the opposite channels versus the radiation spot's actual position: (a) $U_B - U_C$ and $(U_B - U_C)/(U_B + U_C)$ versus the position along the X axis; (b) $U_A - U_D$ and $(U_A - U_D)/(U_A + U_D)$ versus the position along the Y axis. ($X = 0, Y = 0$) is the middle of the photosensitive area.

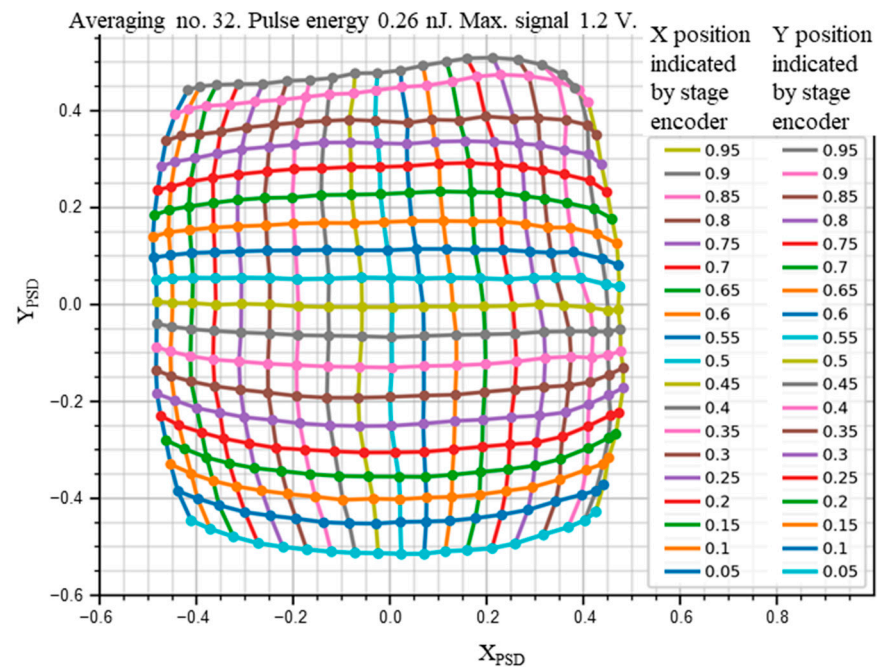


Figure 21. PSD position error chart (adapted with permission from Ref. [20]; copyright: 2022, SPIE). Colored curves with the $(X_{\text{PSD}}, Y_{\text{PSD}})$ points are assigned by color to the respective actual position (X, Y) values, given in two columns at the right. The encoders were zeroed at the corner of the area, so the central point is $(X = 0.5, Y = 0.5)$, corresponding to $(X_{\text{PSD}} = 0, Y_{\text{PSD}} = 0)$. The PSD module sample #1.

In Figure 17, the map of the sum of all four outputs shows the periphery with $> 30\%$ of the signal attenuation, covering about half of the photosensitive area. This may be caused by the radiation spot extending partially outside the photosensitive area. In addition, other nonuniformities are clearly visible, also on subsequent maps in Figures 18 and 19, taken for the signal from each PSD channel separately. No anti-etaloning solutions were applied, so etaloning due to radiation interferences in the wide-gap layers outside the absorber might contribute here. Inhomogeneities of the material layers, particularly the resistive layer, the cathode electrode metal–semiconductor contact, and the absorber and its interfaces may also play a role. Slightly more uniform maps were obtained for the next sample of the PSD module #2 (Figure 19).

Figure 20 plots linear scan results as the difference between the signals from the opposite channels versus the radiation spot's actual position given by the encoders. Also shown is the interesting known linearization effect when the difference between the signals is divided by their sum. The linearization hides the nonuniformities visible in the plots of the simple difference (Figure 20a).

It was also interesting to measure a map of the difference, or error, between the $(X_{\text{PSD}}, Y_{\text{PSD}})$ spot position determined from the PSD signals, using Equations (1) and (2), and the actual (X, Y) position given by the encoders. This is shown in Figure 21. The noise was merely visible due to the 32 averaging no. used. Nonlinearities are clearly visible, with barrel-like shapes characteristic of the tetra-lateral configuration of the cathode electrodes [13].

7. Noise Characterization

Figure 22 illustrates primary noise contributions for a typical connection of the PSD and the ROC. $\overline{u_{nA}}$, $\overline{u_{nB}}$, $\overline{u_{nC}}$, and $\overline{u_{nD}}$ at the respective outputs are the roots of the sum of the signal variances from uncorrelated noise sources.

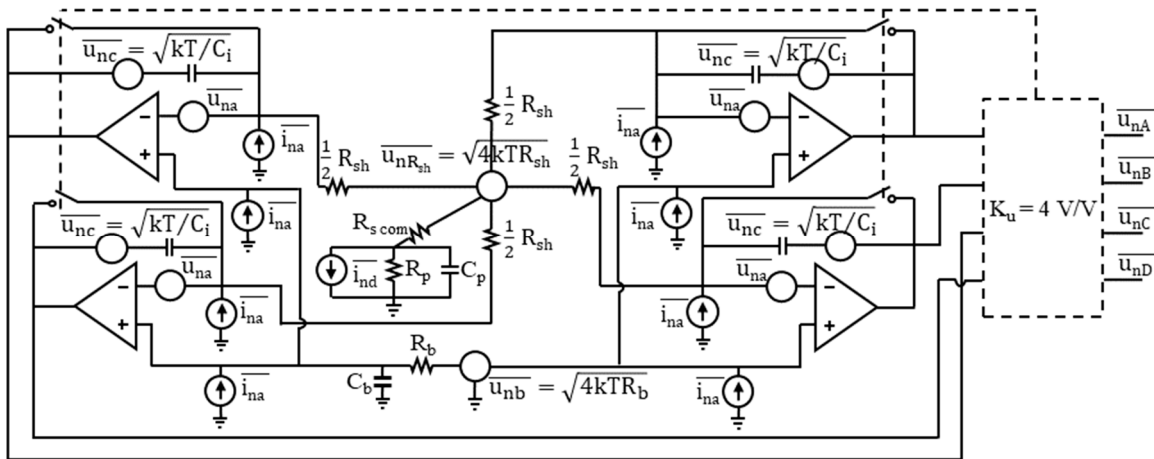


Figure 22. Noise sources, rms, based on the connection diagram shown in Figure 11 and the detector's equivalent circuit shown in Figure 7: $\overline{u_{na}}$ and $\overline{i_{na}}$ are the voltage and current, respectively, noise spectral densities of the preamplifier input; $\overline{u_{nb}}$ and $\overline{u_{nR_{sh}}}$ are the noise voltage spectral densities of the bias voltage source and the resistive layer sheet resistance, respectively; $\overline{u_{nc}}$ is the noise voltage of the thermal fluctuations of the charge left on the integrating capacitor after opening an ideal switch.

The output noise is estimated under the following assumptions: the dark condition; the detector dark current is spread evenly between the four cathode electrodes A, B, C, and D, with the dark current per channel $I_{d/ch} = 12 \text{ mA}$ at $V_b = 0.16 \text{ V}$; and the voltage and current rms noises of the preamplifier input, $\overline{u_{na}} = 1 \text{ nV}/\sqrt{\text{Hz}}$ and $\overline{i_{na}} = 2.8 \text{ pA}/\sqrt{\text{Hz}}$, respectively, are the same for all the preamplifiers used. Then, the same formula may be used for the total rms of the fluctuations Q_{nA} , Q_{nB} , Q_{nC} , and Q_{nD} of the charges Q_A , Q_B , Q_C , and Q_D , respectively, integrated during the CDS time interval τ_{CDS} on the capacitance $C_i = 220 \text{ pF}$ of the respective channels, and for the resulting noises $\overline{u_{nA}}$, $\overline{u_{nB}}$, $\overline{u_{nC}}$, and $\overline{u_{nD}}$:

$$\overline{Q_{nA}} = \sqrt{\tau_{CDS} \int_{-\infty}^{+\infty} (2eI_{d/ch}g_{ph} (1 + f_k^{1.1}/f^{1.1}) / (1 + f_1^{1.1}/f^{1.1}) + 4kT_d/R_{sh} + \overline{u_{na}}^2/|Z_d|^2 + \overline{i_{na}}^2) \text{sinc}^2(\pi f \tau_{CDS}) df + kT_e C_i} \quad (11)$$

where $g_{ph} = 1.7$ is estimated according to Equation (7); f_k is the $1/f$ noise higher crossover (knee) frequency, below which the $1/f$ noise dominates; $f_k = 1 \text{ MHz}$ is fit to the measured PSD photodiode noise current spectral density $\overline{i_{nd}}$, shown in Figure 23, where $0.5 \times \overline{i_{nd}} = \overline{i_{nd/ch}}$; the 1.1 exponent at the f_k and the frequency variable f is a result of fit to the measured $\overline{i_{nd}}$ in the range, where the $1/f$ noise dominates; several f_1 values are assumed, where f_1 is the $1/f$ noise lower crossover frequency related to the time of the measurement [63], i.e., to τ_{CDS} ; $T_d = 205 \text{ K}$; $T_e = 295 \text{ K}$ is the operating temperature of the preamplifier; $Z_d = R_{sh}/2 + [(j2\pi f C_p)^{-1} \parallel R_p]$; k is the Boltzmann constant; and e is the charge of the electron.

The high $C_b = 100 \text{ }\mu\text{F}$ capacity connected in parallel with the V_b voltage source with the internal resistance $R_b = 50 \text{ }\Omega$ limits the noise bandwidth at the output of the V_b voltage source to only $1/(4C_b R_b) = 50 \text{ Hz}$. This makes the noise of this source negligible, so it is not included in Equation (11).

The output noise voltage is calculated as follows:

$$\overline{u_{nA}} = \overline{u_{nB}} = \overline{u_{nC}} = \overline{u_{nD}} = \sqrt{\left(\frac{Q_{nA}}{C_i} \times K_u\right)^2 + \overline{u_{nOSC}}^2} \quad (12)$$

where $K_u = 4 \text{ V/V}$ is the gain of the output stage of the preamplifier (Figures 11 and 22) and $\overline{u_{nOSC}}$ is the vertical (voltage) rms noise of the oscilloscope for a given volt/div setting applied.

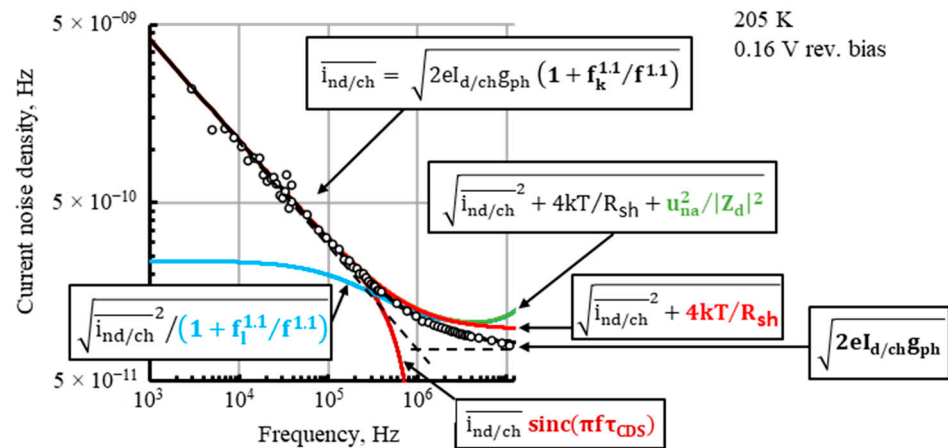


Figure 23. Contributors to the noise current spectral density on the integrating capacitor of the PSD module. The measured dark current noise density per one channel $\overline{i_{nd/ch}}$ is marked in black. Other respective highlighted expressions were calculated and taken from Equation (11). Components with $\text{sinc}(\pi f \tau_{CDS})$ and f_1 factors are shown for $\tau_{CDS} = 1 \mu\text{s}$, where f_1 is assumed to equal $1/(2\pi\tau_{CDS})$.

There could be some negative correlation between the respective noise contributions in the u_{nA} , u_{nB} , u_{nC} , and u_{nD} output noises originating from thermal (Johnson) noise of the resistive layer. This correlation is expected to increase with the PSD photodiode parallel impedance $Z_p = R_p \parallel (j2\pi f C_p)^{-1}$. However, the contribution of the Johnson noise of the resistive layer is insignificant due to the limited noise bandwidth imposed by the CDS integrating interval τ_{CDS} through the $\text{sinc}(\pi f \tau_{CDS})$ transfer function and because of domination of the huge $1/f$ noise of the PSD photodiode. This is shown in Figure 23, demonstrating several contributions to the noise current spectral density on the integrating capacitor. The black line fits points of half of the measured PSD photodiode noise current spectral density, $\overline{i_{nd/ch}} = 0.5 \times \overline{i_{nd}}$, obtained with all the cathode outputs connected together, before integration of the PSD with electronics, and the red line provides the same noise with the added calculated Johnson noise current spectral density of the resistive layer. The contribution of the preamplifier input voltage noise spectral density $\overline{u_{na}}$, i.e., $\overline{u_{na}}/|Z_d|$ noise current spectral density, is insignificant too, for the same reason.

In addition, $\overline{i_{na}} = 2.8 \text{ pA}/\sqrt{\text{Hz}}$, $\overline{u_{nOSC}} = 165 \mu\text{V}$, and $\sqrt{kT_e C_i}/C_i \times K_u = 17 \mu\text{V}$ are negligible.

The blue line in Figure 23 demonstrates strong limitation to the noise by the $1/f$ noise lower crossover frequency f_1 assumed to equal $1/(2\pi\tau_{CDS})$, as in [64]. Following [63], f_1 should be in inverse proportion to the measurement time, equal to τ_{CDS} here, and the value of f_1 can be obtained from measurements or a theory. The output noise voltage estimated by Equations (11) and (12) for the integration time $\tau_{CDS} = 1 \mu\text{s}$ and $0.5 \mu\text{s}$ and for the several values of f_1 is given in Figure 24.

The output noise voltage measurement was carried out using the ROC and PSD connections from Figure 11 and a fast oscilloscope operated at 10 GigaSamples/second and 500 MHz bandwidth. The CDS technique described in Section 6 was used and no laser light was applied, so no photosignal was produced. Figure 25 is a histogram of the CDS voltages measured at $\tau_{CDS} = 1 \mu\text{s}$ and with the PSD operated at $V_b = 0.16 \text{ V}$ and $T_d = 205 \text{ K}$. The Gaussian-like distributions of the CDS voltage with its rms noises $\overline{u_{nA}} = 3.6 \text{ mV}$, $\overline{u_{nB}} = 3.4 \text{ mV}$, $\overline{u_{nC}} = 3.5 \text{ mV}$, and $\overline{u_{nD}} = 3.6 \text{ mV}$ at the respective outputs were obtained. The measured values for the rms noise were 1.6 times greater than the output noise voltage estimated by Equations (11) and (12) for the same τ_{CDS} and conditions of PSD operation if $f_1 = 1/(2\pi\tau_{CDS})$ was assumed, as in [64]. This is still reasonably good consistency between the measured and estimated noise values.

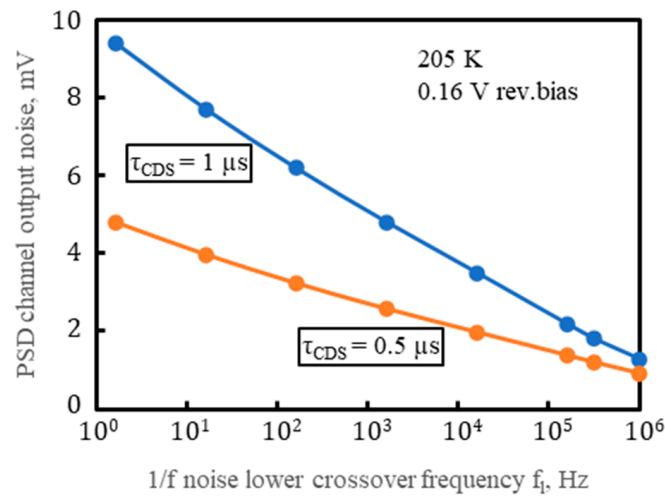


Figure 24. The output noise voltage estimated by Equations (11) and (12) for the integration time $\tau_{CDS} = 1 \mu s$ and $0.5 \mu s$ and for the several values of the $1/f$ noise lower crossover frequency f_1 (adapted with permission from Ref. [20]; copyright: 2022, SPIE).

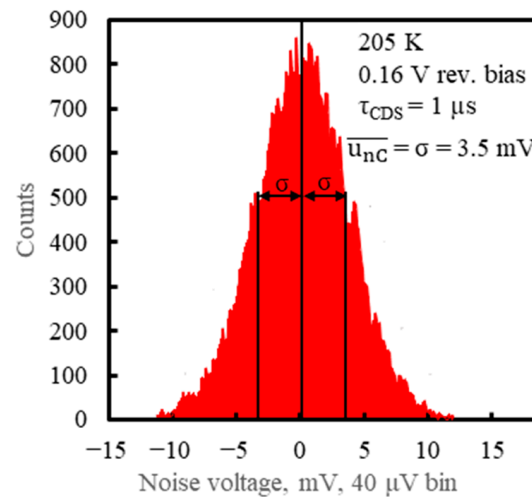


Figure 25. Histogram of the CDS noise voltage u_{nC} , measured at the output C of the PSD module (adapted with permission from Ref. [20]; copyright: 2022, SPIE).

Finally, the measurement resolution of the (X_{PSD}, Y_{PSD}) position was determined, $\overline{x_{nPSD}}$ and $\overline{y_{nPSD}}$, based on:

- Equations (3) and (4);
- The measured noise of the output voltage;
- The output signals measured for the positions of the radiation spot where the maximum difference between the signals from the opposite cathode electrodes occurred, i.e., beyond the central area where a similar or better resolution was achieved.

The data are summarized in Table 3. The position resolution of $3\text{--}6 \mu m$ without averaging was obtained using the τ_{CDS} interval of $1 \mu s$ and $0.26 \text{ nJ } 100 \text{ ns}$ radiation pulses. However, the photocurrent was actually integrated just during the 100 ns radiation pulse. For the radiation pulse wider than the applied CDS interval, the photocurrent was integrated 10 times longer, over the entire interval $\tau_{CDS} = 1 \mu s$, and the signal-to-noise ratio also increased 10 times. Thus, the position resolution of this PSD is 10 times better, i.e., $0.3\text{--}0.6 \mu m$.

Table 3. Output parameters of the PSD module, measured at the maximal difference between the signals from the opposite channels. The PSD module sample #1. No averaging. (adapted with permission from Ref. [20]; copyright: 2022, SPIE).

Condition	Max ($U_A - U_D$)	Max ($U_D - U_A$)	Max ($U_B - U_C$)	Max ($U_C - U_B$)
Direct Measurand				
X, mm	−0.25	0.10	0.40	−0.55
Y, mm	0.40	−0.35	−0.10	−0.10
U_A , V	0.97	0.46	0.37	0.36
$\overline{u_{nA}}$ rms, V, dark noise	3.6×10^{-3}	3.6×10^{-3}	3.6×10^{-3}	3.6×10^{-3}
U_B , V	0.44	0.76	0.82	0.26
$\overline{u_{nB}}$ rms, V, dark noise	3.4×10^{-3}	3.4×10^{-3}	3.4×10^{-3}	3.4×10^{-3}
U_C , V	0.67	0.56	0.30	0.87
$\overline{u_{nC}}$ rms, V, dark noise	3.5×10^{-3}	3.5×10^{-3}	3.5×10^{-3}	3.5×10^{-3}
U_D , V	0.40	1.23	0.52	0.45
$\overline{u_{nD}}$ rms, V, dark noise	3.6×10^{-3}	3.6×10^{-3}	3.6×10^{-3}	3.6×10^{-3}
Indirect measurand				
$U_A - U_D$, V	0.57	−0.78	−0.15	−0.09
$(U_A - U_D)/E_{in}$, V/J	2.2×10^9	-3.0×10^9	-5.7×10^8	-3.5×10^8
$U_B - U_C$, V	−0.23	0.20	0.52	−0.62
$(U_B - U_C)/E_{in}$, V/J	-8.8×10^8	7.5×10^8	2.0×10^9	-2.4×10^9
$Y_{PSD} = (U_A - U_D)/(U_A + U_D) \times 1$, mm	0.41	−0.46	−0.17	−0.11
$\overline{y_{nPSD}}$ rms, μm	4.0	3.3	5.8	6.3
$X_{PSD} = (U_B - U_C)/(U_B + U_C) \times 1$, mm	−0.21	0.15	0.47	−0.55
$\overline{x_{nPSD}}$ rms, μm	4.4	3.7	4.8	4.8

This position resolution could be further improved with modest averaging. Averaging improves signal-to-noise ratio $N^{1/2}$ times, where N is the averaging number. Thus, the resolution is improved $N^{1/2}$ times, too, according to Equations (3) and (4). The measurement time equal to $\tau_{CDS} = 1 \mu\text{s}$ plus a few microseconds for resetting would be increased N times then.

Using Equation (6), taking the dark current noise density per one channel $i_{nd/ch}(1 \text{ kHz}) = 4.1 \times 10^{-9} \text{ A/Hz}^{1/2}$ (Figure 23) and the dark current per one channel at the applied reverse bias $I_{d/ch} = 12 \text{ mA}$ (Figure 8), we obtain the $1/f$ noise related Tobin coefficient:

$$\alpha = 4.1 \times 10^{-9} \frac{\text{A}}{\sqrt{\text{Hz}}} \times \frac{\sqrt{1000 \text{ Hz}}}{0.012 \text{ A}} = 1.1 \times 10^{-5} \quad (13)$$

which is a relatively small value compared to some other data from the last few years reported for HgCdTe devices at higher operating temperatures, e.g., for an MOCVD grown MWIR barrier detector at 205 K— $\alpha = 2.7 \times 10^{-4}$ [54] and for a liquid phase epitaxy (LPE) grown MWIR photodiode at 290 K— $\alpha = 2\text{--}40 \times 10^{-5}$ [65]. However, this may reflect not so much the quality of our photodiode as the larger share of the diffusion current in its dark current. Referring to diffusion-current-limited LPE MWIR and LWIR photodiodes at temperatures $\geq 200 \text{ K}$ [66], $\alpha \approx 2 \times 10^{-6}$ can be found.

However, dislocations intercepting the junction are likely to be a challenge, limiting the production yield of our relatively large $1 \times 1 \text{ mm}^2$ photodiodes. The probability of a dislocation intercepting the junction is proportional to the dislocation density and the junction area. We obtained the $1 \text{ mm} \times 1 \text{ mm}$ photodiodes with yields a few times lower

compared to devices with a smaller photosensitive area of $100\ \mu\text{m} \times 100\ \mu\text{m}$. The defective detectors had high dark currents and too-low resistances.

8. Summary and Conclusions

The lateral-effect position-sensitive Peltier-cooled LWIR detector was recently demonstrated [20] for the first time to the authors' knowledge and described in more detail here. It was based on a modified PIN HgCdTe photodiode with a spectral sensitivity range of 3–11 μm , forming the tetra-lateral PSD with a photosensitive area of $1 \times 1\ \text{mm}^2$. The device was coupled to integrating preamplifiers and scanned with a focused radiation beam. It was capable of achieving a position resolution of 0.3–0.6 μm using a box-car integration time of 1 μs with correlated double sampling, which dramatically reduced the noise bandwidth and limited the contribution of the huge $1/f$ noise of this photodiode and the offsets of the output signal.

In order to improve the position linearity of this PSD, the cause of the observed nonuniformities in the signal maps should be further clarified, e.g., by comparison with maps obtained with a thermal radiation source. Anti-etaloning solutions should be considered. Inhomogeneities of the on-chip material layers, particularly the resistive layer, can be overcome by improving chip processing. However, the input impedance of integrating op-amps is comparable to and greater than the resistive layer sheet resistance, limiting the PSD performance, and differences between op-amp chips may also play a role. To avoid this, it is required to increase the impedance of the photodiode and the resistance of the resistive layer accordingly.

Due to the low yield and higher-than-expected thermal G-R, TAT, and resulting $1/f$ noise of this PSD, our technology should be investigated for improving dislocation density and surface passivation.

A 20-fold decrease in the dark current compared to the level exhibited by this PSD, possible with the fully depleted absorber, could significantly reduce the $1/f$ noise. Another way to avoid or lessen the $1/f$ noise is to minimize the depletion volume, e.g., with 0 V biased inter-band cascade infrared photodetectors based on InAs/InAsSb superlattices [50] or biased barrier devices, such as nBn made of HgCdTe [51], both optimized for suitably high resistance and fast response.

Resetting the integrating capacitor extends the time between position measurements to a few microseconds. With sufficiently low noise, non-integrating op-amps can be used that do not require resetting between measurements, allowing full use of the small time constant of this PSD, provided that the lead wire inductance is lowered according to the increased operating frequency.

Author Contributions: Conceptualization, J.P. (Jarosław Pawluczyk) and J.P. (Józef Piotrowski); Methodology, J.P. (Jarosław Pawluczyk) and M.Ż.; Validation, J.P. (Jarosław Pawluczyk), M.Ż. and J.P. (Józef Piotrowski); Formal analysis, J.P. (Jarosław Pawluczyk); Investigation, J.P. (Jarosław Pawluczyk) and M.Ż.; Resources, J.P. (Jarosław Pawluczyk) and M.Ż.; Data curation, J.P. (Jarosław Pawluczyk); Writing—original draft, J.P. (Jarosław Pawluczyk); Writing—review & editing, J.P. (Jarosław Pawluczyk), M.Ż. and J.P. (Józef Piotrowski); Visualization, J.P. (Jarosław Pawluczyk); Supervision, J.P. (Jarosław Pawluczyk) and J.P. (Józef Piotrowski). All authors have read and agreed to the published version of the manuscript.

Funding: This study has been supported by contract between VIGO Photonics S.A. in Poland and ASML Netherlands B.V.

Data Availability Statement: Data available within the article.

Acknowledgments: The authors appreciate helpful regular discussions with Roel Pouls and Wim van der Zande during the development of the device and help from Anton Montagne at the electronics design beginning from its concept and preliminary simulations.

Conflicts of Interest: The device was made and tested using the proprietary technology of VIGO Photonics S.A. in Poland. The authors declare no conflict of interest.

References

1. Related Documents | Two-Dimensional PSDs | Hamamatsu Photonics. Available online: https://www.hamamatsu.com/eu/en/product/optical-sensors/distance-position-sensor/psd/two-dimensional-psd/related_documents.html (accessed on 17 March 2023).
2. Chrzanowski, K.; Rogalski, A. Infrared Devices and Techniques (Revision). *Metrol. Meas. Syst.* **2014**, *10*, 565–618.
3. Applications. Available online: <https://vigophotonics.com/knowledge-base/applications/> (accessed on 17 March 2023).
4. Rogalski, A. *Infrared and Terahertz Detectors*, 3rd ed.; CRC Press: Boca Raton, FL, USA; Taylor & Francis Group: Boca Raton, FL, USA, 2019; ISBN 978-1-138-19800-5.
5. Calibrated Thermal Position & Power Sensors. Available online: https://www.thorlabs.com/newgrouppage9.cfm?objectgroup_id=13545 (accessed on 27 March 2023).
6. Wolfshagen, R.; Smith, E.P.G.; Beuville, E.J.; Wilcox, M.; Venzor, G.M.; Peterson, J.M.; Reddy, M.; Wehner, J.G.A.; Ramirez, A.M.; Johnson, S.M.; et al. HgCdTe Position Sensitive Detector (PSD) Development. In *Infrared Technology and Applications XXXVI*; Andresen, B.F., Fulop, G.F., Norton, P.R., Eds.; SPIE: Orlando, FL, USA, 2010; Volume 7660, p. 76600H.
7. Andersson, H. Position Sensitive Detectors—Device Technology and Applications in Spectroscopy. Ph.D. Thesis, Mid Sweden University, Sundsvall, Sweden, 2008.
8. Hu, C.; Wang, X.; Song, B. High-Performance Position-Sensitive Detector Based on the Lateral Photoelectrical Effect of Two-Dimensional Materials. *Light Sci. Appl.* **2020**, *9*, 88. [[CrossRef](#)] [[PubMed](#)]
9. Mäkynen, A. Position-Sensitive Devices and Sensor Systems for Optical Tracking and Displacement Sensing Applications. Ph.D. Thesis, University of Oulu, Oulu, Finland, 2000.
10. Schottky, W. On the Origins of Photoelectrons in Cu₂O-Cu Photocells. *Phys. Z* **1930**, *31*, 913–925.
11. Wallmark, J. A New Semiconductor Photocell Using Lateral Photoeffect. *Proc. IRE* **1957**, *45*, 474–483. [[CrossRef](#)]
12. Lucovsky, G. Photoeffects in Nonuniformly Irradiated P-n Junctions. *J. Appl. Phys.* **1960**, *31*, 1088–1095. [[CrossRef](#)]
13. Woltring, H.J. Single- and Dual-Axis Lateral Photodetectors of Rectangular Shape. *IEEE Trans. Electron Devices* **1975**, *22*, 581–590. [[CrossRef](#)]
14. Petersson, G.P.; Lindholm, L.-E. Position Sensitive Light Detectors with High Linearity. *IEEE J. Solid-State Circuits* **1978**, *13*, 392–399. [[CrossRef](#)]
15. Lampton, M.; Carlson, C.W. Low-distortion Resistive Anodes for Two-dimensional Position-sensitive MCP Systems. *Rev. Sci. Instrum.* **1979**, *50*, 1093–1097. [[CrossRef](#)]
16. Detector Types PVM, PVMQ and PCQ in Catalog of Products of VIGO Photonics, S.A. Available online: <https://vigophotonics.com/knowledge-base/files/> (accessed on 17 March 2023).
17. Pawluczyk, J.; Sosna, A.; Wojnowski, D.; Koźniewski, A.; Romanis, M.; Gawron, W.; Piotrowski, J. Higher Operation Temperature Quadrant Photon Detectors of 2–11 μm Wavelength Radiation with Large Photosensitive Areas. In *Technologies for Optical Countermeasures XIV*; SPIE: Warsaw, Poland, 2017; Volume 10435, p. 1043505.
18. Qiao, S.; Liu, J.; Fu, G.; Wang, S.; Ren, K.; Pan, C. Laser-Induced Photoresistance Effect in Si-Based Vertical Standing MoS₂ Nanoplate Heterojunctions for Self-Powered High Performance Broadband Photodetection. *J. Mater. Chem. C* **2019**, *7*, 10642–10651. [[CrossRef](#)]
19. Position Sensing Detectors. Available online: https://www.thorlabs.com/newgrouppage9.cfm?objectgroup_id=4400 (accessed on 27 March 2023).
20. Pawluczyk, J.; Zbik, M.F.; Piotrowski, J. Peltier Cooled LWIR Lateral Effect Position Sensitive HgCdTe Photodetector. In *Quantum Sensing and Nano Electronics and Photonics XVIII*; Razeghi, M., Ed.; SPIE: San Francisco, CA, USA, 2022; Volume PC12009, p. PC1200906.
21. Cui, S.; Soh, Y.C. Linearity Indices and Linearity Improvement of 2-D Tetralateral Position-Sensitive Detector. *IEEE Trans. Electron Devices* **2010**, *57*, 2310–2316. [[CrossRef](#)]
22. Pawluczyk, J.; Piotrowski, J.; Pusz, W.; Koźniewski, A.; Orman, Z.; Gawron, W.; Piotrowski, A. Complex Behavior of Time Response of HgCdTe HOT Photodetectors. *J. Electron. Mater.* **2015**, *44*, 3163–3173. [[CrossRef](#)]
23. Ashley, T.; Elliott, C.T.; White, A.M. Non-Equilibrium Devices for Infrared Detection. In *Infrared Technology XI*; Mollicone, R.A., Spiro, I.J., Eds.; SPIE: San Diego, CA, USA, 1985; Volume 0572, p. 123.
24. Kinch, M.A. *Fundamentals of Infrared Detector Materials*; Tutorial Texts Series; SPIE Press: Bellingham, WA, USA, 2007; ISBN 978-0-8194-6731-7.
25. Piotrowski, J.; Rogalski, A. *High-Operating-Temperature Infrared Photodetectors*; SPIE: Bellingham, WA, USA, 2007; ISBN 978-0-8194-6535-1.
26. Sah, C.; Noyce, R.N.; Shockley, W. Carrier Generation and Recombination in P-N Junctions and P-N Junction Characteristics. *Proc. IRE* **1957**, *45*, 1228–1243. [[CrossRef](#)]
27. Rosencher, E.; Mosser, V.; Vincent, G. Transient-Current Study of Field-Assisted Emission from Shallow Levels in Silicon. *Phys. Rev. B* **1984**, *29*, 1135–1147. [[CrossRef](#)]
28. Józwiowski, K.; Kopytko, M.; Rogalski, A.; Józwiowska, A. Enhanced Numerical Analysis of Current-Voltage Characteristics of Long Wavelength Infrared n-on-p HgCdTe Photodiodes. *J. Appl. Phys.* **2010**, *108*, 074519. [[CrossRef](#)]
29. Kinch, M.A.; Strong, R.L.; Schaake, C.A. 1/f Noise in HgCdTe Focal-Plane Arrays. *J. Electron. Mater.* **2013**, *42*, 3243–3251. [[CrossRef](#)]

30. Józwiowski, K.; Józwiowska, A.; Kopytko, M.; Rogalski, A.; Jaroszewicz, L.R. Simplified Model of Dislocations as a SRH Recombination Channel in the HgCdTe Heterostructures. *Infrared Phys. Technol.* **2012**, *55*, 98–107. [CrossRef]
31. Davis, A.P.; Elliott, C.T.; White, A.M. Current Gain in Photodiode Structures. *Infrared Phys.* **1991**, *31*, 575–577. [CrossRef]
32. Józwiowski, K.; Józwiowska, A. Enhanced Numerical Modeling of HgCdTe Long Wavelength Infrared Radiation High Operating Temperature Non-Equilibrium $P^+v(\pi)N^+$ Photodiodes. *J. Electron. Mater.* **2019**, *48*, 6030–6039. [CrossRef]
33. Humphreys, R.G. Radiative Lifetime in Semiconductors for Infrared Detection. *Infrared Phys.* **1986**, *26*, 337–342. [CrossRef]
34. Hooge, F.N. $1/f$ Noise Sources. *IEEE Trans. Electron Devices* **1994**, *41*, 1926–1935. [CrossRef]
35. Burstein, E.; McWhorter, A.L.; Miller, P.H.; Stevenson, D.T.; Weisz, P.B. *Semiconductor Surface Physics*; University of Pennsylvania Press: Philadelphia, PA, USA, 1957; ISBN 978-0-8122-7113-3.
36. Black, R.D.; Weissman, M.B.; Restle, P.J. $1/f$ Noise in Silicon Wafers. *J. Appl. Phys.* **1982**, *53*, 6280–6284. [CrossRef]
37. Van der Ziel, A. Semiclassical Derivation of Handel's Expression for the Hooge Parameter. *J. Appl. Phys.* **1988**, *63*, 2456–2457. [CrossRef]
38. Józwiowski, K.; Józwiowska, A.; Martyniuk, A. Dislocations as a Noise Source in LWIR HgCdTe Photodiodes. *J. Electron. Mater.* **2016**, *45*, 4769–4781. [CrossRef]
39. Gross; Sodini. $1/f$ Noise in MOSFETs with Ultrathin Gate Dielectrics. In Proceedings of the 1992 International Technical Digest on Electron Devices Meeting, San Francisco, CA, USA, 13–16 December 1992; IEEE: San Francisco, CA, USA, 1992; pp. 881–884.
40. Tobin, S.P.; Iwasa, S.; Tredwell, T.J. $1/f$ Noise in (Hg, Cd)Te Photodiodes. *IEEE Trans. Electron Devices* **1980**, *27*, 43–48. [CrossRef]
41. Hsu, S.T. Surface State Related $1f$ Noise in P-n Junctions. *Solid-State Electron.* **1970**, *13*, 843–855. [CrossRef]
42. Lee, D.; Carmody, M.; Piquette, E.; Dreiske, P.; Chen, A.; Yulius, A.; Edwall, D.; Bhargava, S.; Zandian, M.; Tennant, W.E. High-Operating Temperature HgCdTe: A Vision for the Near Future. *J. Electron. Mater.* **2016**, *45*, 4587–4595. [CrossRef]
43. Kinch, M.A.; Wan, C.-F.; Schaake, H.; Chandra, D. Universal $1/f$ Noise Model for Reverse Biased Diodes. *Appl. Phys. Lett.* **2009**, *94*, 193508. [CrossRef]
44. Schiebel, R.A. A Model for $1/f$ Noise in Diffusion Current Based on Surface Recombination Velocity Fluctuations and Insulator Trapping. *IEEE Trans. Electron Devices* **1994**, *41*, 768–778. [CrossRef]
45. Anderson, W.W.; Hoffman, H.J. Surface-tunneling-induced $1/f$ Noise in $Hg_{1-x}Cd_xTe$ Photodiodes. *J. Vac. Sci. Technol. A* **1983**, *1*, 1730–1734. [CrossRef]
46. Józwiowski, K.; Piotrowski, J.; Józwiowska, A.; Kopytko, M.; Martyniuk, P.; Gawron, W.; Madejczyk, P.; Kowalewski, A.; Markowska, O.; Martyniuk, A.; et al. The Numerical–Experimental Enhanced Analysis of HOT MCT Barrier Infrared Detectors. *J. Electron. Mater.* **2017**, *46*, 5471–5478. [CrossRef]
47. Baker, I.; Maxey, C.; Hipwood, L.; Weller, H.; Thorne, P. Developments in MOVPE HgCdTe Arrays for Passive and Active Infrared Imaging. In *Electro-Optical Remote Sensing, Photonic Technologies, and Applications VI*; SPIE: Edinburgh, UK, 2012; Volume 8542, p. 85421A.
48. Baker, I.M.; Maxey, C.D. Summary of HgCdTe 2D Array Technology in the U.K. *J. Electron. Mater.* **2001**, *30*, 682–689. [CrossRef]
49. Lee, D.; Dreiske, P.; Ellsworth, J.; Cottier, R.; Chen, A.; Tallaricao, S.; Yulius, A.; Carmody, M.; Piquette, E.; Zandian, M.; et al. Law 19: The Ultimate Photodiode Performance Metric. In *Infrared Technology and Applications XLVI*; SPIE: Online Only, 2020; Volume 11407, p. 114070X.
50. Gawron, W.; Kubiszyn, Ł.; Michalczewski, K.; Manyk, T.; Piotrowski, J.; Martyniuk, P. The Performance of the ICIP Ga-Free Superlattice Longwave Infrared Photodetector for High Operating Temperature. *Infrared Phys. Technol.* **2023**, *128*, 104499. [CrossRef]
51. Benyahia, D.; Martyniuk, P.; Kopytko, M.; Antoszewski, J.; Gawron, W.; Madejczyk, P.; Rutkowski, J.; Gu, R.; Faraone, L. NBn HgCdTe Infrared Detector with HgTe(HgCdTe)/CdTe SLS Barrier. *Opt. Quantum Electron.* **2016**, *48*, 215. [CrossRef]
52. ADA4896-2 Datasheet and Product Info | Analog Devices. Available online: <https://www.analog.com/en/products/ada4896-2.html> (accessed on 12 December 2022).
53. Tennant, W.E.; Lee, D.; Zandian, M.; Piquette, E.; Carmody, M. MBE HgCdTe Technology: A Very General Solution to IR Detection, Described by “Rule 07”, a Very Convenient Heuristic. *J. Electron. Mater.* **2008**, *37*, 1406–1410. [CrossRef]
54. Ciura, Ł.; Kopytko, M.; Martyniuk, P. Low-Frequency Noise Limitations of InAsSb-, and HgCdTe-Based Infrared Detectors. *Sens. Actuators Phys.* **2020**, *305*, 111908. [CrossRef]
55. Inductance of a Straight Wire: A Calculator. Available online: <http://www.consultrsr.net/resources/eis/induct5.htm> (accessed on 12 December 2022).
56. Grover, F.W. *Inductance Calculations: Working Formulas and Tables*; Instrument Society of America: Research Triangle Park, NC, USA, 1981; ISBN 978-0-87664-557-4.
57. IVC102 | Buy TI Parts | TI.Com. Available online: <https://www.ti.com/product/IVC102/part-details/IVC102U> (accessed on 11 December 2022).
58. Żbik, M.; Wiczorek, P.Z. Versatile Subnanosecond Laser Diode Driver. In *Photonics Applications in Astronomy, Communications, Industry, and High-Energy Physics Experiments 2016*; Romaniuk, R.S., Ed.; SPIE: Wilga, Poland, 2016; Volume 10031, p. 100311F.
59. Żbik, M.; Wiczorek, P. Charge-Line Dual-FET High-Repetition-Rate Pulsed Laser Driver. *Appl. Sci.* **2019**, *9*, 1289. [CrossRef]
60. Żbik, M.; Szatkowski, J.; Wiatr, W. Time-Domain Characterization of High-Speed Mid-Infrared Photodetectors Using a Laser-Based Non-Linear Vector Network Analyzer System. In Proceedings of the 23rd International Microwave and Radar Conference (MIKON), Warsaw, Poland, 5–7 October 2020; pp. 263–267.

61. Hougen, C.A. Model for Infrared Absorption and Transmission of Liquid-phase Epitaxy HgCdTe. *J. Appl. Phys.* **1989**, *66*, 3763–3766. [[CrossRef](#)]
62. Gawron, W.; Damięcki, A.; Koźniewski, A.; Martyniuk, P.; Stasiewicz, K.A.; Madejczyk, P.; Rutkowski, J. Multiple Long Wavelength Infrared MOCVD Grown HgCdTe Photodetectors for High Temperature Conditions. *IEEE Sens. J.* **2021**, *21*, 4509–4516. [[CrossRef](#)]
63. Niemann, M.; Kantz, H.; Barkai, E. Fluctuations of $1/f$ Noise and the Low-Frequency Cutoff Paradox. *Phys. Rev. Lett.* **2013**, *110*, 140603. [[CrossRef](#)]
64. Gordon, N.T. Thermo Electrically Cooled Focal Plane Arrays Based on MCT. In *Infrared Technology and Applications XXXVI*; Andresen, B.F., Fulop, G.F., Norton, P.R., Eds.; SPIE: Orlando, FL, USA, 2010; Volume 7660, p. 76602X.
65. Guinedor, P.; Brunner, A.; Rubaldo, L.; Bauza, D.; Reibold, G.; Billon-Lanfrey, D. Low-Frequency Noises and DLTS Studies in HgCdTe MWIR Photodiodes. *J. Electron. Mater.* **2019**, *48*, 6113–6117. [[CrossRef](#)]
66. Hassis, W.; Gravrand, O.; Rothman, J.; Benahmed, S. Low-Frequency Noise Characteristics of HgCdTe Infrared Photodiodes Operating at High Temperatures. *J. Electron. Mater.* **2013**, *42*, 3288–3296. [[CrossRef](#)]

Disclaimer/Publisher's Note: The statements, opinions and data contained in all publications are solely those of the individual author(s) and contributor(s) and not of MDPI and/or the editor(s). MDPI and/or the editor(s) disclaim responsibility for any injury to people or property resulting from any ideas, methods, instructions or products referred to in the content.